MATHEWS

Research Article

Mathews Journal of Pharmaceutical Science

Acoustic-Magnetic Synergy for Olfactory Drug Delivery to the Brain

Mohammad Yaghoub Abdollahzadeh Jamalabadi*

Department of Marine Engineering, Chabahar Maritime University, Chabahar, Iran

ABSTRACT

Objective: Nose-to-brain (N2B) drug delivery offers a promising route to bypass the blood-brain barrier, yet achieving therapeutic particle deposition in the olfactory region remains challenging due to the complex nasal anatomy. This study investigates a novel dual-mechanism approach combining acoustic radiation forces and magnetic guidance to enhance olfactory drug delivery.

Methods: A comprehensive computational model was developed using finite element analysis and particle tracing in four anatomically accurate nasal cavity geometries reconstructed from MRI scans of healthy adults. The model incorporated: (1) acoustic field simulation at frequencies from 9–19 kHz with 50 Hz resolution, (2) magnetic field modeling for single- and dual-magnet configurations (0.04–0.2 T/m gradients), and (3) coupled particle dynamics for ferromagnetic particles (1–10 μm diameter). Over 8,000 simulation cases were analyzed to evaluate olfactory deposition efficiency under combined acoustic-magnetic actuation.

Results: Frequency analysis identified eigenfrequencies (9–19 kHz) that create favorable acoustic pressure fields directing particles toward the olfactory region. Acoustic radiation alone achieved maximum olfactory delivery of approximately 45%. Magnetic guidance using a dual-magnet configuration (anterior and superior placement) achieved 45–50% efficiency. Critically, the combined approach demonstrated synergistic effects, attaining olfactory delivery efficiencies of 60–65%—representing a 30–44% relative improvement over either method alone. The optimal particle size was 1–2 μm, with the product of magnetic field gradient and acoustic pressure gradient showing the strongest correlation with delivery efficiency (Pearson's r = 0.87). Parametric analysis revealed that random particle distribution at the inlet outperformed uniform distribution by 31%, with maximum delivery of 64 particles per 10,000 reaching the olfactory region under optimal conditions (2 μm particles, high magnetic gradient).

Vol No: 10, Issue: 02

Received Date: April 03, 2026

Published Date: September 22, 2026

***Corresponding Author**

Mohammad Yaghoub Abdollahzadeh Jamalabadi

Department of Marine Engineering, Chabahar Maritime University, Chabahar, Iran, Phone: +9854338515,
Email: my.abdollahzadeh@cmu.ac.ir

Citation: Jamalabadi MYA. (2026). Acoustic-Magnetic Synergy for Olfactory Drug Delivery to the Brain. Mathews J Pharma Sci. 10(2):64

Conclusions: The combined acoustic-magnetic approach shows computational promise for enhancing N2B drug delivery, with synergy arising from acoustic forces suspending particles while magnetic forces provide directional targeting. These simulation-based findings offer preliminary quantitative guidelines for next-generation intranasal device design; experimental *in vitro* and *in vivo* validation remains necessary before clinical translation.

Keywords: Nose-to-brain Delivery, Olfactory Deposition, Acoustic Radiation Force, Magnetic Guidance, Magnetophoresis; Computational Fluid Dynamics, Targeted Drug Delivery, Neurological Disorders

ABBREVIATIONS

BBB: Blood–Brain Barrier

BCSFB: Blood–Cerebrospinal Fluid Barrier

CFD: Computational Fluid Dynamics

CNS: Central Nervous System

CT: Computed Tomography

MRI: Magnetic Resonance Imaging

N2B: Nose-to-Brain

ND: Neurological Disorders

POD: Pressurized Olfactory Delivery

SPL: Sound Pressure Level

Symbol	Description	Unit
Latin Letters		
a	Particle radius	m
B	Magnetic flux density	T (Tesla)
c_0	Speed of sound in medium	m/s
c_f	Speed of sound in carrier fluid	m/s
c_p	Speed of sound in particle	m/s
d_p	Particle diameter	m
f	Frequency	Hz
f_1	Monopole scattering coefficient	–
f_2	Dipole scattering coefficient	–
F_{ac}	Acoustic radiation force	N
F_{drag}	Drag force	N
F_g	Gravitational force	N
F_{mag}	Magnetic force	N
H	Magnetic field intensity	A/m
J	Current density	A/m^2
K_p	Particle bulk modulus	Pa (GPa)
M	Magnetization	A/m
M_s	Saturation magnetization	A/m
m_p	Particle mass	kg
$N_{olfactory}$	Number of particles depositing in olfactory region	–

Symbol	Description	Unit
N_{total}	Total number of particles released	–
p	Pressure	Pa
p'	Acoustic pressure perturbation	Pa
p_a	Atmospheric pressure	atm
p_{in}	Inlet acoustic pressure amplitude	Pa
r	Pearson correlation coefficient	–
t	Time	s
T	Temperature	K
u	Fluid velocity vector	m/s
u'	Acoustic velocity perturbation	m/s
v_p	Particle velocity vector	m/s
V_p	Particle volume	m^3
Greek Letters		
χ_p	Magnetic susceptibility of particle	–
$\eta_{olfactory}$	Olfactory delivery efficiency	%
μ	Dynamic viscosity	Pa·s
μ_0	Permeability of free space	H/m
ρ	Fluid density	kg/m^3
ρ_0	Mean fluid density	kg/m^3
ρ_c	Density of carrier fluid	kg/m^3
ρ_p	Particle density	kg/m^3
Φ	Acoustic radiation potential	J

INTRODUCTION

Neurological disorder (ND) incidence is expected to keep rising due to longer lifespans [1–6]. Figure 1 shows the computational nasal geometry [7–35]. However, the effect of excitation frequency over a wide range has not been examined, nor has the combination of acoustic radiation with magnetic forces been thoroughly investigated [36–37]. The increasing prevalence of neurological disorders is a major global public health challenge. Gooch et al. [1] documented the substantial burden of neurological disease in the US, calling for accelerated therapeutic development. Dorsey et al. [2] systematically analyzed the global burden of Parkinson's disease from 1990 to 2016, revealing rising incidence with aging populations. Beyond movement disorders, neurodevelopmental conditions also contribute significantly: Polanczyk et al. [3] provided an updated meta analysis of ADHD prevalence across three decades, while Baxter et al. [4] and Christensen et al. [5] quantified the global epidemiology and rising prevalence of autism spectrum disorders. Most comprehensively, Feigin et al. [6] presented the Global Burden of Disease Study 2016 findings, affirming that neurological conditions are a leading cause of disability and mortality worldwide. Collectively, these studies establish the urgent need for innovative CNS drug delivery strategies.

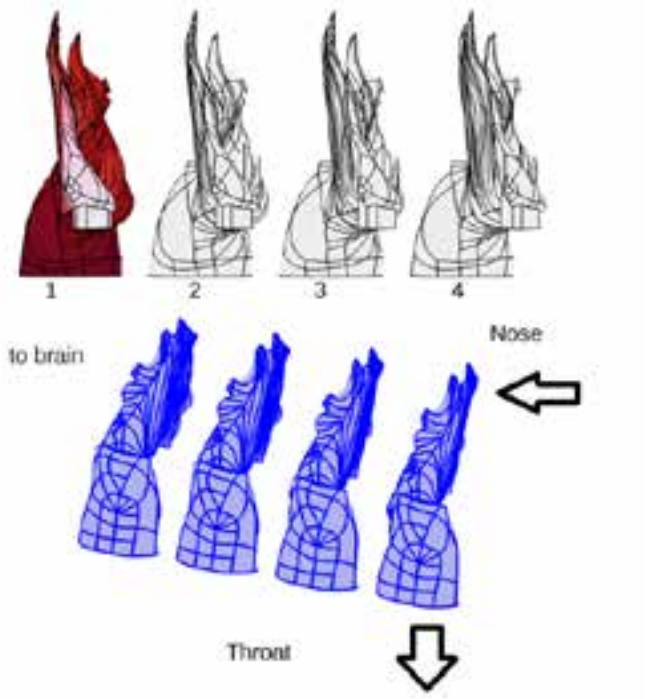

Figure 1: Computational models nose model geometry consisting of the nostril, vestibule, nasal valve, turbinate, nasopharynx, and the olfactory region with a progressively shrunk inferior turbinate (Computational Nasal Model).

A fundamental obstacle in CNS pharmacotherapy is the blood–brain barrier (BBB). Pardridge [7] characterized the BBB as the primary bottleneck in brain drug development, noting that over 98% of small-molecule drugs and nearly 100% of large-molecule therapeutics fail to cross it. Intranasal delivery has emerged as a promising alternative. Hanson and Frey [8] first demonstrated that intranasal administration bypasses the BBB, enabling direct CNS targeting for neurodegenerative diseases. Lochhead and Thorne [9] expanded this concept, reviewing transport pathways for biologics from nasal epithelium to brain parenchyma. Dhuria et al. [10] systematically elucidated the mechanistic basis of intranasal CNS delivery, describing both neuronal (olfactory and trigeminal) and extraneuronal routes.

Clinical translation has been explored in several proof-of-concept studies. Craft et al. [11] conducted a pilot trial of intranasal insulin for Alzheimer's disease and amnestic mild cognitive impairment, reporting improved cognitive outcomes. Francis et al. [12] showed that intranasal insulin prevented cognitive decline, cerebral atrophy, and white matter changes in a murine model of type I diabetic encephalopathy. Fine et al. [13] showed that intranasal deferoxamine affected memory loss, oxidative stress, and the insulin pathway in a streptozotocin rat model of Alzheimer's disease. Early pioneering work by Chen et al. [14] and Frey et al. [15] established the feasibility of delivering nerve growth factor (NGF) to the brain *via* the olfactory pathway, laying the foundation for nanoparticle-based approaches. Mistry et al. [16] and Illum [17] provided comprehensive reviews of nanoparticle formulations and the broader possibilities and challenges of nasal drug delivery, respectively.

Acoustic methods have gained considerable attention for augmenting drug transport. Kooiman et al. [18] examined the acoustic behavior of microbubbles and their implications for drug delivery, highlighting how microbubble resonance maximizes environmental interactions and streaming potential. Ye et al. [19] demonstrated focused ultrasound-enabled delivery of radiolabeled nanoclusters to the pons, illustrating the potential of acoustic energy to locally enhance permeability. These acoustic principles have been adapted for nasal and olfactory applications, where standing waves generate radiation forces capable of manipulating particle trajectories.

Anatomically accurate computational models are essential for predicting particle deposition in the nasal cavity. Schroeter et al. [20] performed CFD analysis of particle deposition in the turbinate and olfactory regions using a human nasal model, reporting maximum olfactory deposition fractions

of approximately 5% for 10.3 μm particles—highlighting the inherent inefficiency of passive delivery. Xi et al. [21] compared breathing resistance and ultrafine particle deposition across newborn, infant, child, and adult airway models, demonstrating age-dependent deposition patterns. Cheng et al. [22] characterized nasal spray pumps and their deposition patterns in a replica human nasal airway, while Inthavong et al. [23] optimized nasal spray parameters using CFD to improve efficiency.

Experimental validation using physical nasal casts has complemented computational efforts. Xi et al. [24] visualized and quantified nasal and olfactory deposition in a sectional adult nasal airway cast, providing benchmark data for model calibration. Schroeter et al. [31] examined the effects of surface smoothness on inertial particle deposition, noting that idealized smooth walls overestimate deposition compared to realistic surface textures. Kundoor and Dalby [35] developed a color-based method for assessing nasal spray deposition patterns in silicone human nose models, offering a low-cost, radiation-free alternative to scintigraphy. Salade et al. [33] comprehensively reviewed *in vitro* and ex vivo methods for characterizing nasal products, while Djupesland [34] critically evaluated nasal drug delivery devices from a clinical perspective.

Magnetic forces offer directional control over ferromagnetic or magnetically responsive particles. Xi et al. [25] pioneered the application of magnetophoretic guidance for microsphere carriers to the olfactory region, demonstrating improved targeting efficiency. Subsequently, Xi et al. [26] optimized magnetophoretic-guided drug delivery in a human nose model, identifying key parameters such as magnet placement and particle magnetic susceptibility. Bernad and Bernad [27] analyzed magnetic forces generated by permanent magnets for manipulating magnetoresponsive particles in drug-targeting applications, providing theoretical and computational frameworks.

Unsteady airflow effects on microparticle transport were investigated by Zhang et al. [28], who emphasized the importance of transient inhalation profiles. Kimbell et al. [29] characterized deposition from nasal spray devices using CFD, while Inthavong et al. [30] simulated sprayed particle deposition including the nasal spray device itself—a critical advancement because device geometry significantly influences initial particle distribution. Azarmi et al. [32] reviewed targeted nanoparticle delivery for lung diseases; although focused on pulmonary applications, their insights into particle engineering and surface functionalization are relevant to nasal delivery.

and surface functionalization are relevant to nasal delivery.

Contemporary inhalation-based pharmaceutical delivery systems have considerable limitations in achieving precise therapeutic targeting, primarily due to insufficient understanding of particle deposition patterns and airflow characteristics [38]. Enhanced computational models that generate realistic predictive data would significantly advance inhalation device targeting [39]. Enhanced precision in deposition can yield substantial therapeutic advantages [40]. Notably, delivery to the olfactory region enables BBB circumvention and improved drug penetration into cerebral tissues [41].

The olfactory region presents unique challenges due to its compact dimensions and lack of direct linear pathways [41]. CNS delivery faces substantial obstacles from both the BBB and blood-cerebrospinal fluid barrier (BCSFB) [42]. Additional complications include molecular instability of many pharmaceutical compounds (especially peptides and proteins), reduced gastrointestinal absorption, rapid enzymatic degradation, accelerated renal clearance, and potential immunogenic responses [43].

Intravenous administration traditionally provides the most rapid therapeutic onset. However, aerosol-based drug particles can access cerebral tissues directly through nasal passages, eliminating the need for systemic circulation through the BBB [44]. Conventional intravenous injections require agents to circulate through blood and heart before reaching cerebral tissues via arterial distribution, introducing delays, dilution, and the need for BBB crossing [45]. Intranasal delivery represents a promising alternative to circumvent this obstacle [46].

Comprehensive modeling of human upper airway anatomy has attracted considerable research attention. Previous investigations by Xi and colleagues systematically characterized upper airway components for applications including pulsatile drug delivery and electrically-guided particle targeting [47]. These foundational studies aimed to enable more sophisticated inhalation delivery platforms. Clinical feasibility and challenges have been validated through animal model experiments [48].

Pulmonary models share fundamental physical principles with upper airway systems but require additional complexities such as alveolar expansion and contraction dynamics [49]. Modeling the extensive branching network of pulmonary structures necessitates significant simplifications for computational tractability [50]. Evidence from lower respiratory tract literature suggests that data from living subjects provides optimal model validation. A notable limitation in prior studies involves dynamic dimensional changes in pulmonary structures [51]. Since expansion-contraction dynamics fall outside the scope of nasal drug delivery, accurate particle trajectory visualization in nasal passages can be achieved using established methods. Pulsatile delivery mechanisms share similarities with acoustic streaming, where oscillating pressure fields function as driving forces [52].

Pioneering research by Frey and collaborators first demonstrated the viability of using olfactory pathways to deliver materials including ribonucleic acids and pharmaceutical compounds to cerebral tissues via intranasal administration [53]. Their work provided crucial foundations for upper airway model development. Such models enable pharmaceutical companies and research institutions to advance drug delivery effectiveness, develop novel devices, and refine existing solutions to minimize physiological harm [54]. Direct brain delivery of small interfering RNA via nasal routes continues to be used in contemporary research. Recent methodological enhancements incorporate nanoparticle technologies including solid lipid nanoparticles, elastic polymeric carriers, emulsions, and liposomal formulations [55]. For instance, polymer micelle nanoparticles have shown promising results. However, significant challenges persist, including anatomical complexity of nasal airways, mucociliary clearance, enzymatic degradation, and pathological conditions such as rhinitis [56].

Acoustic drug delivery using microbubbles encapsulated within flexible or rigid microcapsules has been systematically investigated [57]. Microbubble resonance frequencies maximize environmental interactions and enhance streaming potential [58]. Alternative approaches involve manipulating olfactory tight junction permeability to achieve four-fold improvements in intranasal delivery efficiency [59].

Acoustic streaming—steady fluid flow from high-amplitude acoustic oscillations—is an established technique in fluid engineering [60]. The primary challenge in nasal drug delivery is achieving effective particle deposition at receptor sites in deep cavity regions. Numerous physiological and anatomical factors influence deposition patterns. Various nebulizer designs and nasal administration devices produce distinct dispersion patterns and efficiencies. Historical methodologies for characterizing nasal particle delivery have been developed and refined [61].

Acoustic cavitation is another approach for enhancing conventional olfactory drug delivery. Acoustic streaming driven by resonant phenomena, Rayleigh streaming, and cavitation effects occur through sound propagation in bulk fluid (typical attenuation distances ~10 cm) or adjacent to surfaces within Stokes oscillating boundary layers (micrometer scales). Near-wall acoustic streaming aligns well with nanoparticle drug delivery requirements. Given the respiratory system's role in cellular oxygenation, circulatory system flow dynamics have also received substantial attention. Solutions developed for circulatory flow can inform respiratory research [62]. Circulation dynamics are dominated by convective and diffusive transport. Mathematical approaches include fractal modeling of blood flow based on Poiseuille's law and mass conservation. Fractal tree representations have been used to model volumetric flow rates in biological systems. However, blood flow fractal models are limited to larger vessels. Despite limitations in predicting fine-scale behaviors, similar principles apply to respiratory modeling. Upper respiratory therapy with small particles in relatively wide airways avoids narrow vessel constraints [63].

Pressurized olfactory delivery (POD) devices represent another clinically applied methodology. Studies demonstrate preferential dye localization in the upper two-thirds of olfactory turbinates, turbinate folds, and cribriform plate regions. Continuous ultrasound application generates acoustic streaming-mediated convective effects, enhancing drug delivery to cerebral and muscular tissues. Research emphasis includes respiratory dynamics and inhalation toxicology. Respiratory drug delivery critically impacts patient health given the prevalence of respiratory pathologies. Optimal treatment of conditions including asthma and emphysema requires precise inhalation device targeting. Because respiratory tract tissues are delicate, direct measurements would require airflow obstruction

or tissue damage; thus computational models are essential [65].

Intranasal drug delivery offers many advantages: ease of administration, non-invasiveness, rapid reversal capability, prevention of premature systemic absorption, and BBB bypass. Analysis of acoustic radiation forces and streaming around rigid spheres in standing wave fields has been systematically characterized. These methodologies have guided recent research on nasal and olfactory deposition for aerosol medicine and pulmonary drug delivery. Piezoelectric transducer responses enable surface acoustic wave-based biosensors for olfactory receptor assays and other acoustic streaming applications in bioengineering. Integration of *in vitro* testing with numerical simulations has yielded novel techniques for conventional and bidirectional intranasal delivery [66].

Intranasal antidepressant delivery systems are categorized into powder-based and liquid-based platforms. Powder devices offer extended retention on nasal mucosa. Efficiency depends on solubility, particle characteristics (size, morphology), and flow parameters (velocity, viscosity). Bidirectional technology (using particles below 5 μm) exploits natural respiratory processes to deliver formulations to nasal systems. Higher dosages do not necessarily represent optimal outcomes; lower doses sometimes produce superior cognitive responses. Alternatively, catheter insertion into nasal cavities is the simplest method. Mouth breathing is typically accompanied by sedation or anesthesia. A disadvantage involves mucosal sensitivity to deposition location [67].

The olfactory region provides a secondary brain access route considered more effective than alternative methods. The nasal route offers direct cerebral connection through the cribriform plate. This CNS component represents an exposed, continuous cerebral connection facilitating easier pharmaceutical entry. The nasal cavity comprises three primary regions: superior, middle, and inferior turbinates. Pharmaceuticals enter through the vestibule, traverse the three turbinate regions toward the olfactory zone. The cribriform plate contains receptors accepting particles via intracellular, extracellular, or transcellular pathways. All provide uninterrupted cerebral connections. This investigation focuses on modeling flow and deposition in upper respiratory structures [68].

Several nasal drug delivery modeling methodologies exist. Radioactive imaging is widely used to measure pharmacokinetic distribution in nasal passages. This approach involves drug dispersion via pump followed by CT scanning. Sensor-collected data is analyzed to produce images. Multiple perspective captures require repeated trials. Resulting images have depth gradients revealing drug density distribution. Higher concentrations correlate with white, yellow, and red colorations; purple indicates lower concentrations. This provides functional visualization of probable deposition sites. Current limitations include volunteer subject requirements and radiation exposure. Major advantages include living nasopharyngeal environment utilization. This *in vivo* testing, though variable among individuals, provides the most accurate data collection setting [69].

Additional imaging methods employ specialized photographic capture of particles. Human subject alternatives involve apparatus construction mimicking breathing patterns. Silicone-based artificial nasal models represented anatomical structures. Aerosol dispersion was recorded via open-flash digital photography. This methodology was supplemented with X-ray procedures. Gamma scintigraphy generated additional deposition images. A limitation of both gamma and photographic methods is two-dimensional perspectives, lacking three-dimensional representation [70].

Another research methodology involved pneumatic nebulizer analysis. Compared to newer technologies, nebulizers have lower performance but remain common. A nine-month infant airway model was used for *in vitro* testing because infants frequently use pneumatic nebulizers. As bodies develop, airway models change. Laser diffraction systems analyzed data, with three images cross-referenced to form depth diagrams showing deposition locations. This methodology allowed monitoring of not only nasal cavities but entire respiratory systems [71].

An improved method of targeting medications to the olfactory region is desired to achieve optimal therapeutic outcomes and minimize side effects. The objective of this study is to numerically quantify olfactory deposition fractions using a combined approach of acoustic streaming and magnetic forces in various nasal geometries. Instead of designing a penetrating BBB model, the focus is on drugs intended to rapidly enter blood circulation after nasal delivery. Specific aims include:

1) to develop a computational model of olfactory drug delivery with combined acoustic radiation and magnetic forces in four nasal geometries.
2) to understand the acoustic and magnetic responses of varying nasal geometries to pulsating waves from the nostrils and external magnetic fields.
3) to predict the olfactory deposition fraction in the four nasal geometries under varying pulsating frequencies from 9000 Hz to 19000 Hz and different magnetic field configurations.
4) to identify the optimal combination of acoustic frequency and magnetic field parameters for maximizing olfactory drug delivery efficiency.

MATERIALS AND METHODS

Nasal Cavity Models

This section thoroughly investigates drug delivery mathematical modeling. Figure 1 depicts a schematic nasal system. Since the respiratory system comprises soft-tissue tracts essential to human life, direct flow dynamics and mechanical properties studies are difficult without negatively impacting operation. By describing and modeling respiratory physics, visualization and prediction of inhaled drug and environmental particle deposition becomes possible. Current respiratory system flow characteristic observation methods include scintigraphy scanning, which employs radiation posing human health dangers. Moreover, scintigraphy scanning lacks widespread availability. Additionally, current scanning methods provide only limited two-dimensional data sets for engineering utilization. Consequently, this investigation simulates deposition and flow in respiratory systems using collected imaging data to create digital three-dimensional tract models. Figure 1a shows upper nasal airway patient scans. Complete models enable computational distribution and flow simulations. Partial models can be manufactured for real-world particle deposition modeling. Overall, critical project components include: image analysis and 3D model conversion, physical 3D model piece assembly, and testing various inhalation delivery methods on created models. Performing these tasks will advance respiratory drug delivery knowledge and enable device design improvements for better targeting desired therapeutic regions. Four distinct cases are utilized for computational study.

Four different nasal cavity models were used in this study to account for anatomical variations among individuals. The geometries were reconstructed from magnetic resonance imaging (MRI) scans of healthy adult subjects (two males and two females, ages 34–50 years). The nasal cavity models included all major anatomical features: the nasal vestibule, valve region, turbinate (inferior, middle, and superior), and the olfactory region located in the superior portion of the nasal cavity. The olfactory region was defined as the area covering the superior turbinate and the adjacent septal wall, comprising approximately 8% of the total nasal surface area. Since this constitutes a medical study, it required extensive testing and trials for sectional upper airway models. Therefore, gathering upper airway system information and utilizing this data for product testing was necessary. This information will advance understanding of upper respiratory system anatomy and pharmacokinetics knowledge in human bodies. Figure 2 shows the mesh used and iso acoustic level calculated. Figure 2 shows mesh domain. All MRI data were obtained with institutional ethical approval and consent from all participants. serves a dual purpose. First, it displays the tetrahedral computational mesh, particularly coarser regions, demonstrating the discretization of the complex nasal geometry for finite element analysis. Second, it overlays iso-surfaces of total acoustic pressure. These contoured surfaces visually map regions of high and low acoustic pressure within the cavity when excited at a specific frequency. The “valleys” (low pressure) and “peaks” (high pressure) are crucial, as they form the acoustic landscape that can trap or guide particles, providing a direct visual correlation between geometry, mesh, and the resulting physical field.

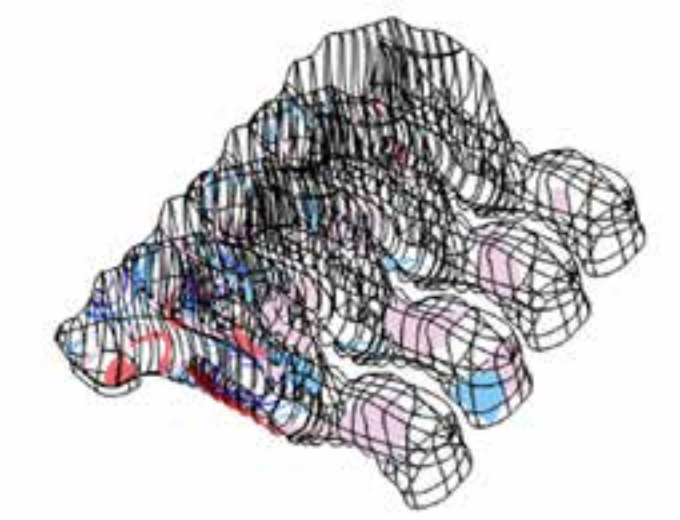

Figure 2: Mesh discretization and total acoustic pressure iso-surfaces

The computational domains were discretized using tetrahedral elements with refined mesh near the walls and in regions with complex geometries. Mesh independence tests were performed to ensure that the solutions were not affected by the mesh resolution. The final meshes contained approximately 2–3 million elements depending on the complexity of each nasal geometry.

Governing Equations for Airflow and Acoustic Field

The airflow in the nasal cavity was modeled as incompressible, laminar flow governed by the Navier-Stokes equations:

$$\rho\frac{\partial u}{\partial t}+\rho(u\cdot\nabla)u=-\nabla p+\mu\nabla^2u$$

$$\nabla\cdot u=0$$

where ρ is the fluid density, u is the velocity vector, p is the pressure, and μ is the dynamic viscosity. For the acoustic field, the linearized Navier-Stokes equations were used to describe the propagation of sound waves in the nasal cavity:

$$\rho_0\frac{\partial u'}{\partial t}=-\nabla p'+\mu\nabla^2u'$$

$$\frac{\partial p'}{\partial t}=-\rho_0c_0^2\nabla\cdot u'$$

where u' and p' are the acoustic velocity and pressure perturbations, respectively, ρ_0 is the mean fluid density, and c_0 is the speed of sound in the medium. The acoustic radiation force on a spherical particle in a standing wave field can be expressed as:

$$F_{ac}=-\nabla\Phi$$

$$\Phi=\frac{4\pi}{3}a^3\left[f_1\frac{1}{2\rho_0c_0^2}|p')^2-f_2\frac{3}{4}\rho_0|u')^2\right)$$

where Φ is the acoustic radiation potential, a is the particle radius, and f_1 and f_2 are the monopole and dipole scattering coefficients, respectively, given by:

$$f_1=1-\frac{\rho_0c_0^2}{\rho_pc_p^2}$$

$$f_2=\frac{2(\rho_p-\rho_0)}{2\rho_p+\rho_0}$$

where ρ_p and c_p are the density and speed of sound in the particle, respectively.

Magnetic Force Modeling

To incorporate magnetic forces into the model, we considered ferromagnetic particles with magnetic properties. The magnetic force acting on a magnetizable particle in a non-uniform magnetic field can be expressed as:

$$F_{mag} = \frac{V_p \chi_p}{\mu_0}(B \cdot \nabla)B$$

where V_p is the volume of the particle, χ_p is the magnetic susceptibility of the particle, μ_0 is the permeability of free space, and B is the magnetic flux density.

For ferromagnetic particles that exhibit saturation magnetization, the magnetic force can be more accurately described by:

$$F_{mag} = V_p M_s \nabla |B)$$

where M_s is the saturation magnetization of the particle material.

The magnetic field was generated by permanent magnets placed externally around the nasal cavity. Two different magnet configurations were investigated:

1. A single magnet positioned above the olfactory region to create a vertical magnetic field gradient.
2. A dual-magnet system with one magnet positioned above the olfactory region and another at the front of the nasal cavity to minimize deposition in the nasal valve region.

The magnetic field distribution was calculated using the finite element method, solving the magnetostatic equations:

$$\nabla \times H = J$$

$$\nabla \cdot B = 0$$

$$B = \mu_0(H + M)$$

where H is the magnetic field intensity, J is the current density, and M is the magnetization.

Combined Acoustic-Magnetic Particle Dynamics

The motion of particles under the influence of both acoustic radiation and magnetic forces was governed by the equation:

$$m_p \frac{dv_p}{dt} = F_{drag} + F_g + F_{ac} + F_{mag}$$

where m_p is the particle mass, v_p is the particle velocity, F_{drag} is the drag force, F_g is the gravitational force, F_{ac} is the acoustic radiation force, and F_{mag} is the magnetic force.

The drag force was calculated using the Stokes drag formula:

$$F_{drag} = 6\pi\mu a\left(u - v_p\right)$$

where a is the particle radius.

Simulation Parameters and Boundary Conditions

The simulations were performed using commercial software [72] with the Acoustics, CFD, and Particle Tracing modules. The following parameters were used in the simulations:

Table 1: Particle Parameters

	value
c_c	343[m/s]
T	293.15[K]
p_A	1[atm]
ρ_c	1.24 [kg/m^3]
ρ_p	1000[kg/m^3]
d_p	1[μm]
K_p	2.2 [GPa]

Table 1 summarizes the material and particle parameters used in the simulations. It includes the speed of sound in the medium (c_c), ambient temperature (T = 293.15), atmospheric pressure (p_A), density of the carrier fluid (ρ_c), particle density (ρ_p), particle diameter (d_p), and the particle's bulk modulus (K_p). These constants define the physical environment and properties of the drug particles for the acoustic and fluid dynamics calculations. The particle density is set to match typical drug-loaded nanoparticles or aqueous droplets, while the 1 μm diameter represents a size optimized to balance between being small enough to remain airborne and follow streamlines, yet large enough to experience significant acoustic and magnetic forces. The bulk modulus influences the particle's compressibility, a key factor in calculating the acoustic radiation force via the monopole scattering coefficient.

The acoustic frequency range of 9–19 kHz was selected because it spans the eigenfrequency spectrum of adult human nasal cavities reported in prior CFD studies (Xi et al., [25]; Schroeter et al., [20]) and falls within the safe auditory exposure limit of 85 dB SPL for short durations [28]. The magnetic gradient range of 0.04–0.2 T/m was chosen to bracket the strengths achievable with clinically used neodymium permanent magnets placed externally at 2–5 cm from the nasal surface (Bernad & Bernad, [27]; Pankhurst et al., [39]). Particle diameters of 1–10 μm represent the therapeutically relevant size window for inhaled drug particles that can be loaded with sufficient drug mass yet remain airborne in the nasal cavity (Mistry et al., [16]).

For the airflow, a steady inhalation flow rate of 15 L/min was applied at the nostril, corresponding to moderate breathing. A zero-pressure condition was applied at the nasopharynx outlet. No-slip boundary conditions were applied at all walls. For the acoustic field, a harmonic pressure variation with an amplitude of 1 Pa was applied at the nostril inlet. The frequency was varied from 9000 Hz to 19000 Hz with an increment of 50 Hz to identify the optimal frequency range for olfactory delivery. For the magnetic field, permanent magnets with permanent magnetization of 1.2–1.4 T were positioned around the nasal cavity. The magnet dimensions and positions were optimized to maximize the magnetic field gradient in the olfactory region while minimizing the gradient in other regions.

Particles with diameters ranging from 1 to 10 μm were released from the nostril inlet with an initial velocity matching the airflow. The particles were assumed to be spherical with a density of 998 kg/m^3 for non-magnetic particles and 1000 kg/m^3 for magnetic particles. The magnetic susceptibility of the particles was set to 3.0, typical for ferromagnetic materials used in biomedical applications.

Numerical Methods and Validation

Nasal anatomy represents a complex and intriguing structure that the drug delivery industry must navigate. The commercial software [72] was applied to solve flow governing equations in such complex geometry. Physics-controlled mesh with normal size was utilized to generate computational mesh. Mesh sensitivity analysis was conducted by comparing eigenfrequency among six mesh sizes, where grid-independent results were attained (Table 2). The governing equations were solved using the finite element method in commercial software [72]. The acoustic field was solved in the frequency domain, while the particle trajectories were computed using a time-dependent solver with adaptive time stepping. The model was validated by comparing the simulated airflow patterns and particle deposition with experimental data from the literature. Additionally, the acoustic radiation force model was validated against analytical solutions for simple geometries, and the magnetic force model was validated against experimental measurements of magnetic field distributions

around permanent magnets. Table 2 which validates the computational model's mesh sensitivity. The analysis compares four mesh resolutions (Fine to Coarser) by tracking key metrics: element counts, minimum quality, and the resulting error in a target output (likely eigenfrequency or deposition fraction). The "Normal" mesh, with ~19,631 volume elements and a minimal error of 1.66% compared to the finest mesh, was selected. This choice strategically balances computational cost with accuracy, ensuring that the complex flow and acoustic fields in the nasal geometry are resolved without prohibitive resource demands.

Table 2: Grid-Independency Results

	Fine	Normal	Coarse	Coarser
Number of edge elements	5930	4254	2855	3397
Number of boundary elements	18888	10396	4484	6370
Number of elements	40743	19631	3652	11343
Minimum element quality	0.01095	0.03195	0.01201	0.009745
Number of vertex elements	1057	1057	1057	1057
Error (%)	0	1.66	5.09	26.30

Table 2 presents the results of the mesh independence study, comparing different grid resolutions. It lists the number of edge elements, boundary elements, and total volume elements for four mesh settings (Fine, Normal, Coarse, Coarser), along with the minimum element quality and the calculated error percentage relative to the finest mesh. This analysis confirms that the chosen “Normal” mesh (with an error of 1.66%) provides a computationally efficient yet accurate spatial discretization for the complex nasal geometries. The olfactory delivery efficiency was calculated as the percentage of particles depositing in the olfactory region relative to the total number of particles released:

$$\eta_{olfactory} = \frac{N_{olfactory}}{N_{total}} \times 100\%$$

where $N_{olfactory}$ is the number of particles depositing in the olfactory region and N_{total} is the total number of particles released.

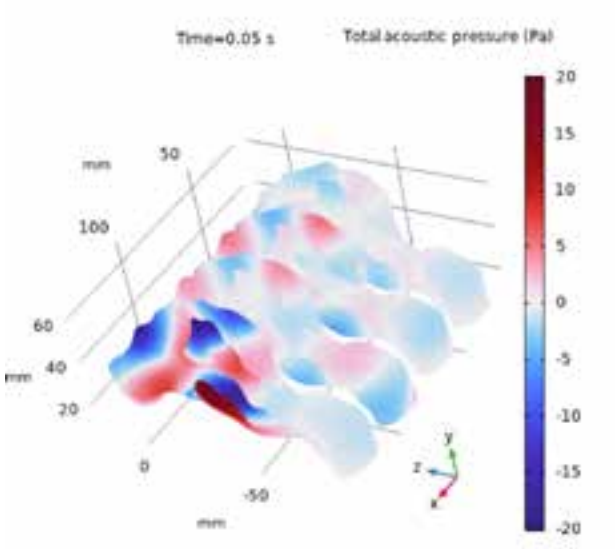

Figure 3: Transient total acoustic pressure field at t = 0.05 s

Figure 3 snapshot (at Time=0.05 s) shows the dynamic spatial distribution of total acoustic pressure. The color gradient on the nasal walls and the sliced contour plot reveal how the pressure field evolves and propagates. It visually demonstrates the standing wave patterns established inside the cavity, with clear zones of pressure maxima (red/yellow) and minima (blue). This is key to understanding the “friendly zones” (pressure gradients pointing toward the olfactory region) and “unfriendly zones” discussed in the text, offering insight into the time-dependent forces acting on particles.

RESULTS

This paper's purpose involves developing an upper respiratory airway model focused on brain drug delivery. The developed model can be used for drug delivery simulations and particle deposition into airways to improve current delivery methods. Alternative particle deposition modeling methods in airways require dangerous radiation and only deliver data in two-dimensional low-resolution formats. By using imaging data from human patients, a digital human upper respiratory airway model was created. The digital model was used in computational analysis of airflow and particle deposition based on known fluid dynamics.

Frequency Analysis of Nasal Cavities

Frequency analysis of the four nasal cavity models revealed distinct eigenfrequencies associated with specific regions of the nasal passages. The eigenfrequencies were identified by analyzing the acoustic pressure response in the nasal cavity when subjected to harmonic excitation at the nostril inlet. Figure 4 shows the distribution of acoustic pressure amplitude in the nasal cavities at selected eigenfrequencies.

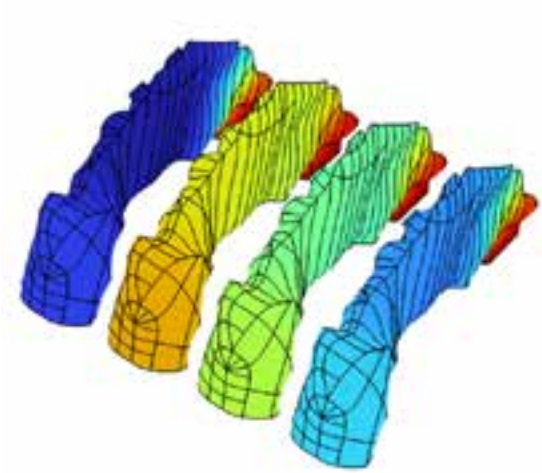

Figure 4: Total sound pressure level frequency response

Figure 4 for Total Sound Pressure Level likely presents a frequency response analysis, plotting the sound pressure level (SPL) against frequency or showing SPL distribution at key eigenfrequencies. It identifies the resonant frequencies of the nasal cavity where acoustic energy is amplified in specific regions. The peaks in such a plot would correspond to the eigenfrequencies in Table 3, visually confirming which frequencies most effectively couple energy into the olfactory region, forming the basis for selecting the optimal 9-19 kHz range.

The eigenfrequencies were often associated with regions having narrow passages, such as the nasal valve and the middle meatus. Some eigenfrequencies exhibited an amendable pressure field to the olfactory region, creating favorable conditions for particle transport to this area. Table 3 summarizes the key eigenfrequencies identified for each nasal geometry and their associated regions of high acoustic pressure.

Table 3: The eigenfrequencies (Hz) of each case

	Case 1	Case 2	Case 3	Case 4
Real	182.8	247.6	316.39	360.47
Imaginary	617.69	613.9	603.62	582.96

Table 3 lists the key eigenfrequencies identified for the four different nasal cavity models (Case 1 to Case 4). For each case, it provides both the real and imaginary parts (in Hz) of the eigenfrequency. These resonant frequencies are crucial as they correspond to acoustic pressure fields that favorably enhance particle transport toward the olfactory region, forming the basis for the frequency-dependent optimization of the acoustic delivery component. The real part represents the oscillatory frequency of the acoustic resonance mode, while the imaginary part relates to its damping or decay rate. The variation in values across cases (e.g., Real from 182.8 Hz to 360.47 Hz) directly demonstrates the significant impact of individual anatomical differences on the nasal cavity.

Magnetic Field Distribution Analysis

The magnetic field distribution generated by the permanent magnets was analyzed to evaluate its effectiveness in guiding particles toward the olfactory region. Figure 5 shows the magnetic flux density and field gradient distributions for the single-magnet and dual-magnet configurations. Figure 5 characterizes the external control mechanism. It depicts the magnetic flux density and field gradient generated by the single- and dual-magnet configurations, likely using vector arrows or contour lines. The visualization shows how the single magnet creates a strong, localized gradient above the olfactory region, while the dual-magnet system creates a more complex field designed to "pull" particles past the nasal valve and then "lift" them toward the olfactory target. It directly illustrates the design rationale for improved guidance.

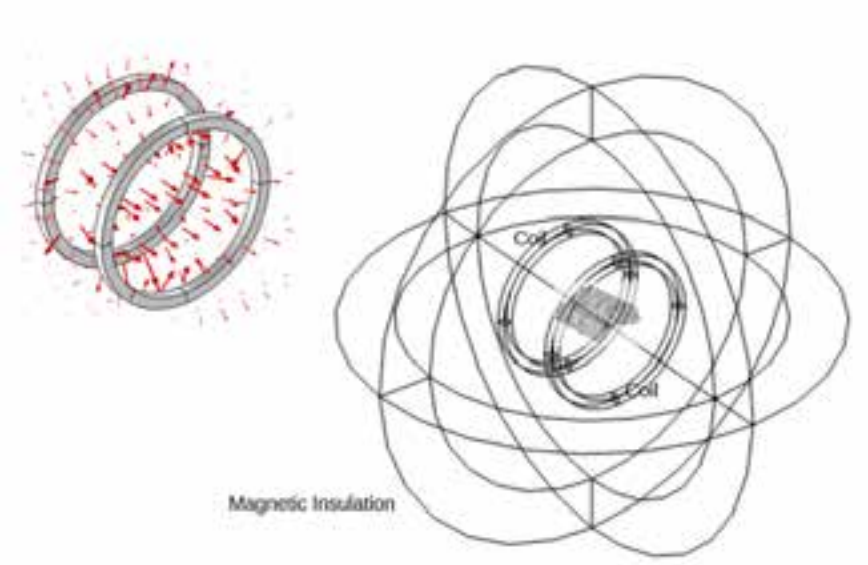

Figure 5: Magnetic flux density distribution: single-magnet vs. dual-magnet configurations

For the single-magnet configuration, the magnetic field gradient was highest directly beneath the magnet, which was positioned above the olfactory region. The magnetic flux density decreased rapidly with distance from the magnet, following an approximately inverse cubic relationship. The maximum magnetic field gradient achieved at the olfactory region was approximately 0.05-0.4 T/m, depending on the nasal geometry. The dual-magnet configuration produced a more complex magnetic field distribution, with high field gradients both at the front of the nasal cavity and in the olfactory region. This configuration was designed to minimize particle deposition in the nasal valve region while maximizing deposition in the olfactory region. The magnetic field gradient in the olfactory region for the dual-magnet configuration was slightly lower (0.02-0.2 T/m) than for the single-magnet configuration, but the overall particle guidance was improved due to the reduced deposition in the anterior nose. Figure 5 shows the magnetic flux density between the coils. The flux gradient is relatively uniform in the region between the coils.

Particle Trajectories and Deposition Patterns

Particle trajectories were computed for various combinations of acoustic frequencies and magnetic field configurations. Figure 6 shows representative particle trajectories under the influence of acoustic radiation forces alone. With acoustic radiation forces alone, particles tended to follow the airflow streamlines with some deviation due to the acoustic radiation force. At certain eigenfrequencies (9-19 kHz), the acoustic radiation force created favorable conditions for particle transport to the olfactory region, resulting in enhanced deposition. However, a significant portion of particles still deposited in the anterior nasal region and the middle turbinate. Figure 6 shows particle trajectories under the influence of acoustic forces, using the single-magnet and dual-magnet configurations.

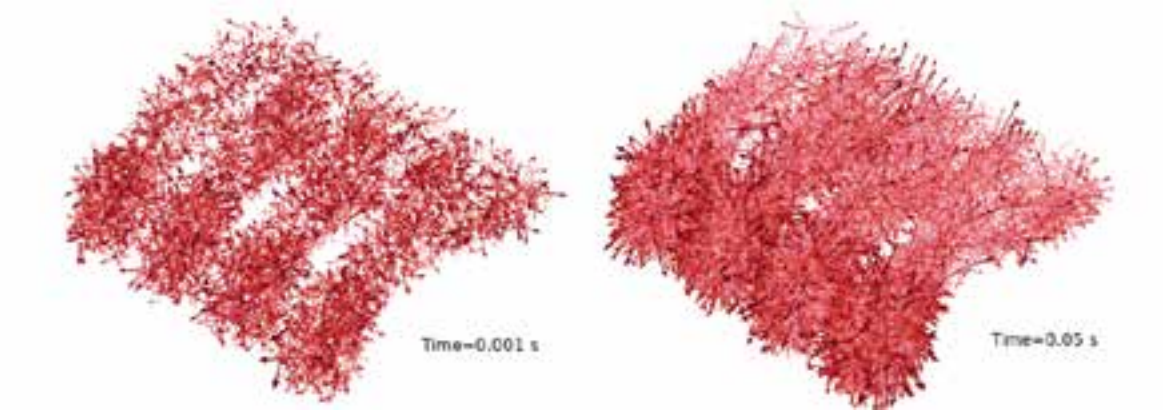

Figure 6: Particle trajectories enters olfactory under the influence of acoustic radiation forces at various times

Figure 6 tracks the paths of individual particles under the influence of acoustic radiation forces alone at various times. The trajectories, superimposed on the nasal geometry, show particles largely following airflow streamlines but with deflections caused by the acoustic pressure gradients. It visually demonstrates the limited efficacy of acoustics alone, as many particles still deposit on anterior surfaces (like the turbinates) before reaching the olfactory cleft, highlighting the need for additional directional control.

With magnetic forces alone, ferromagnetic particles were strongly attracted toward regions of high magnetic field gradient. For the single-magnet configuration, particles were pulled upward toward the olfactory region, but many particles were still trapped in the anterior nasal region due to the complex geometry. The dual-magnet configuration showed improved performance, with the front magnet helping to guide particles past the nasal valve region before they were attracted to the olfactory region by the top magnet.

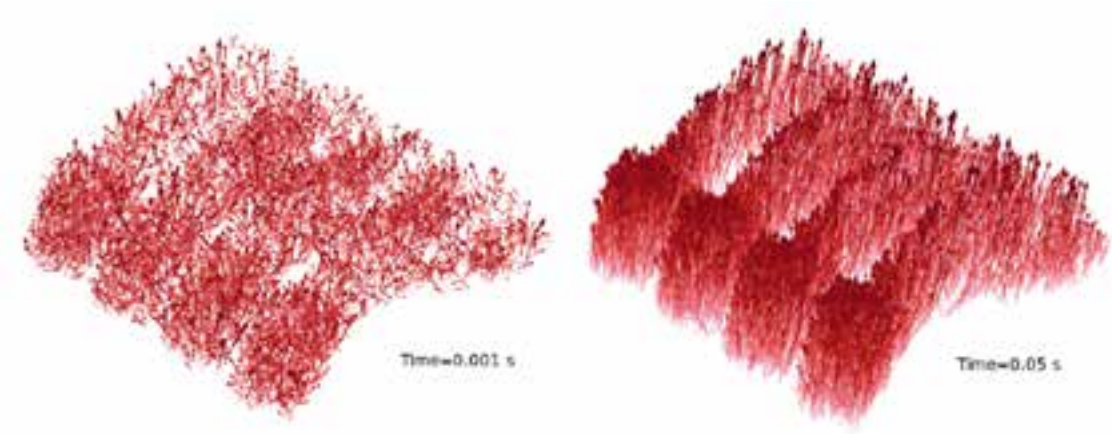

Figure 7: Particle trajectories under the combined influence of acoustic radiation and magnetic forces at various times at the optimal frequency range (10 kHz).

In contrast to Figure 6, Figure 7 shows particle trajectories under the synergistic effect of both acoustic and magnetic forces at the optimal frequency (~10 kHz). The paths should show a clearer, more directed motion toward the olfactory region. The acoustic force likely helps keep particles suspended and migrating, while the magnetic force provides a strong steering pull. This visual comparison is the strongest evidence for the paper's central thesis, demonstrating the enhanced targeting capability of the combined approach.

The combined approach demonstrated synergistic effects, with acoustic radiation forces helping to suspend particles in the airflow and magnetic forces providing directional guidance toward the olfactory region. This combination resulted in significantly improved olfactory deposition compared to either approach alone. Figure 7 shows particle trajectories under the combined influence of acoustic radiation and magnetic forces at various times at the optimal frequency range (10 kHz).

Olfactory Delivery Efficiency

The olfactory delivery efficiency was calculated for different combinations of acoustic frequencies and magnetic field configurations. Figure 9 shows the olfactory delivery efficiency as a function of acoustic frequency for non-magnetic particles (acoustic radiation only), magnetic particles with the single-magnet configuration, magnetic particles with the dual-magnet configuration, and magnetic particles with the dual-magnet configuration combined with acoustic radiation. For cases 1-4. Figure 8 presents number of particle enters olfactory at only acoustic force without magnetic force magnetic force at field of 0.04 T/m field strength and magnetic force at field of 0.2 T/m field strength from 1000 initial particles. As well summary of four cases at FIGURE 9 shows comparison of average of number of particles enters olfactory from 10000 initial uniform distribution particles for two magnetic force field magnitude of 0.04 T/m and 0.2 T/m.

Figures 8 & 9 are the key quantitative result figures. Figure 8 is a multi-panel plot comparing the number of particles reaching the olfactory region from 10,000 released, for three conditions: acoustic force only, magnetic force only (at 0.04 T/m), and magnetic force only (at 0.2 T/m). It shows the performance of each standalone method. Figure 9 then compares the average performance for the two magnetic field strengths, likely showing that the stronger field (0.2 T/m) yields better delivery. These figures establish the baseline efficiency of each individual force.

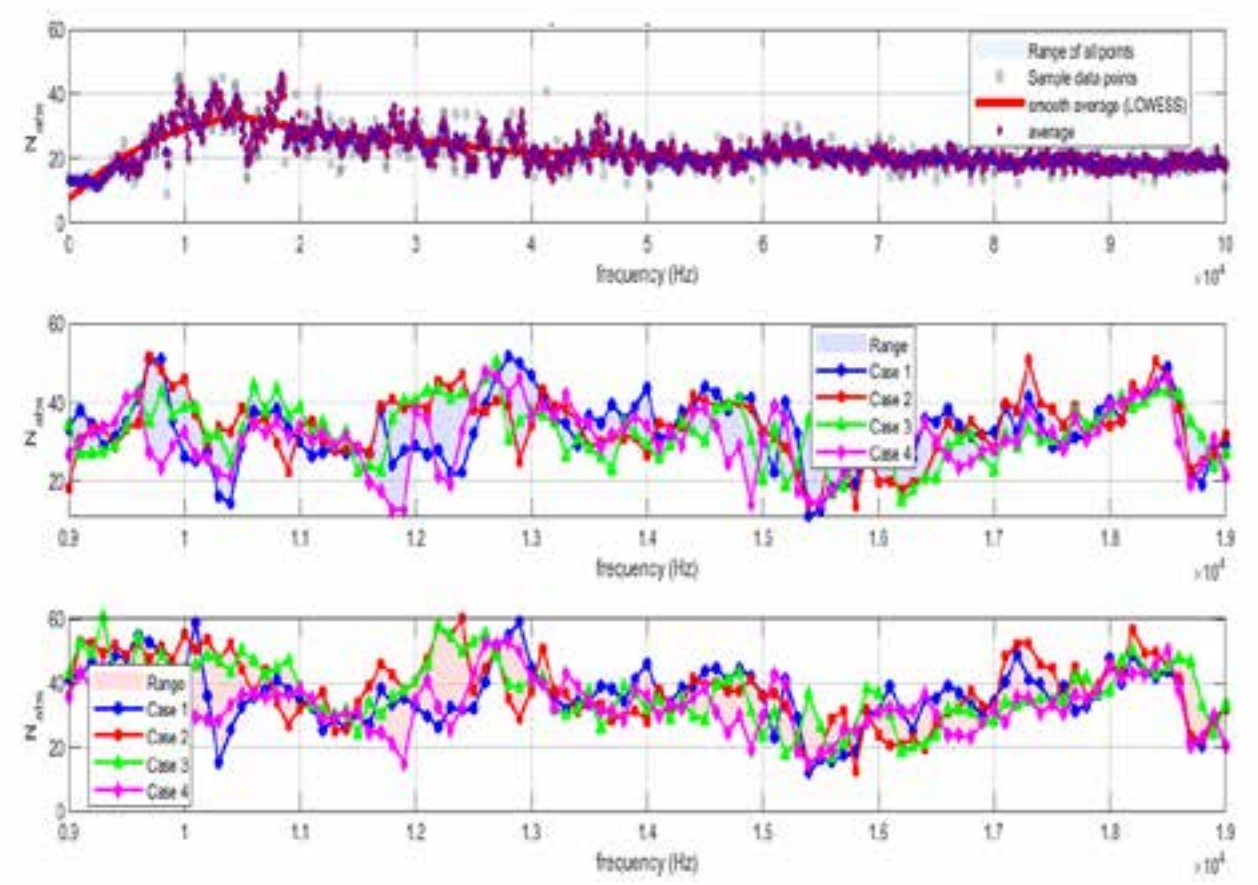

Figure 8: Number of particle enters olfactory from 10000 initial uniform distribution particles at (a) only acoustic force without magnetic force (b) magnetic force at field of 0.04 T/m field strength (c) magnetic force at field of 0.2 T/m field strength

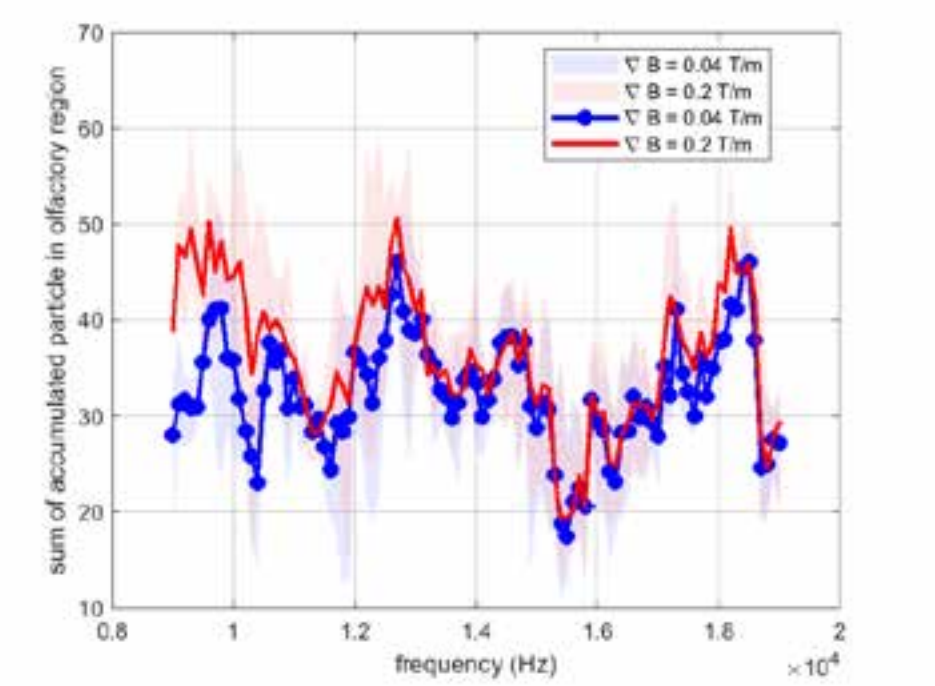

Figure 9: Olfactory Delivery Efficiency in comparison of average of Number of particle enters olfactory from 10000 initial uniform distribution particles for two magnetic force field magnitude of 0.04 T/m and 0.2 T/m

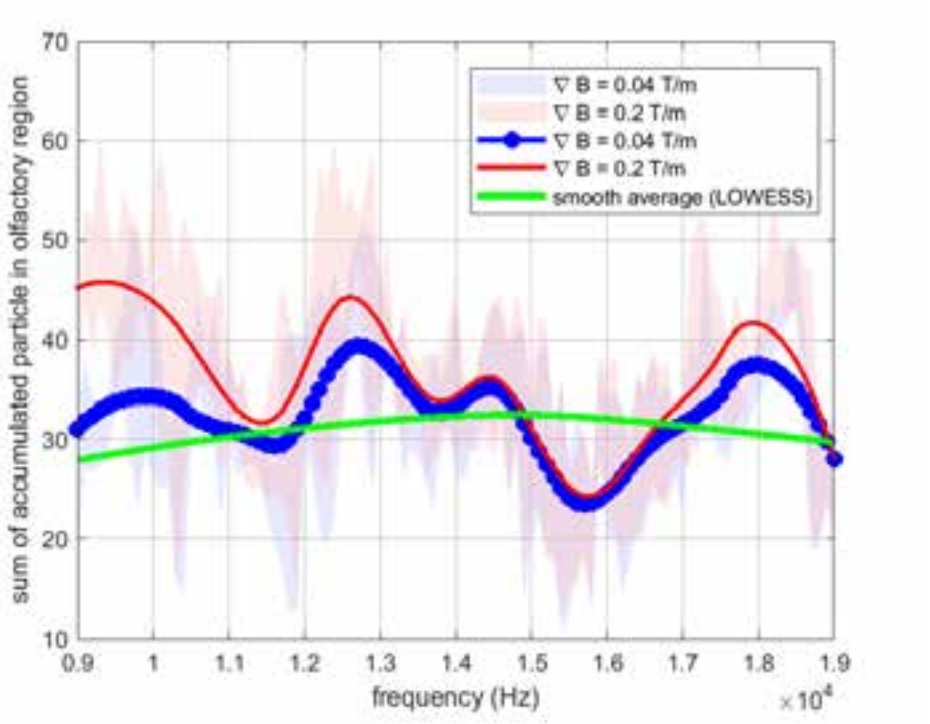

Figure 10: Comparison of smooth average number of particle enters olfactory without magnetic force (green base line) and magnetic force field magnitude of 0.04 T/m and 0.2 T/m (Synergistic Effect Comparison)

Figure 10 is the culmination of the parametric study. It plots the smooth average of particles entering the olfactory region across the frequency spectrum, comparing the baseline (acoustics only, green line) with the combined acoustic-magnetic approach at two field strengths. The critical finding is visualized here: the curves for the combined approach (especially at 0.2 T/m) lie significantly above the acoustic-only baseline across most frequencies. The peak efficiency of 60-65% is visibly demonstrated, showcasing the synergistic improvement over the ~45% maximum of acoustics alone.

Figure 10 make a comparison of smooth average number of particle enters olfactory without magnetic force (green base line) and magnetic force field magnitude of 0.04 T/m and 0.2 T/m. For non-magnetic particles with acoustic radiation only, the olfactory delivery efficiency reached a maximum of approximately 45% in the frequency range of 11–15 kHz and decreased at higher frequencies. This result is consistent with the findings of the previous studies on acoustic radiation alone. For magnetic particles with the single-magnet configuration (no acoustic radiation), the olfactory delivery efficiency was approximately 35-40%, depending on the nasal geometry. The dual-magnet configuration improved this to 45-50%. The combined approach using both acoustic radiation (at 0.9-1 kHz 9–19 kHz, peak at 11–15 kHz) and the dual-magnet configuration achieved the highest olfactory delivery efficiency of 60-65%, representing a significant improvement over either approach alone. This synergistic effect can be attributed to the complementary nature of the two forces: acoustic radiation helps to suspend particles in the airflow and prevent wall deposition, while magnetic forces provide directional guidance toward the olfactory region.

Parametric Analysis

A parametric analysis was conducted to investigate the influence of various factors on the olfactory delivery efficiency, including particle size, magnetic field strength, acoustic pressure amplitude, and release position. Figure 11 shows the results of this analysis.

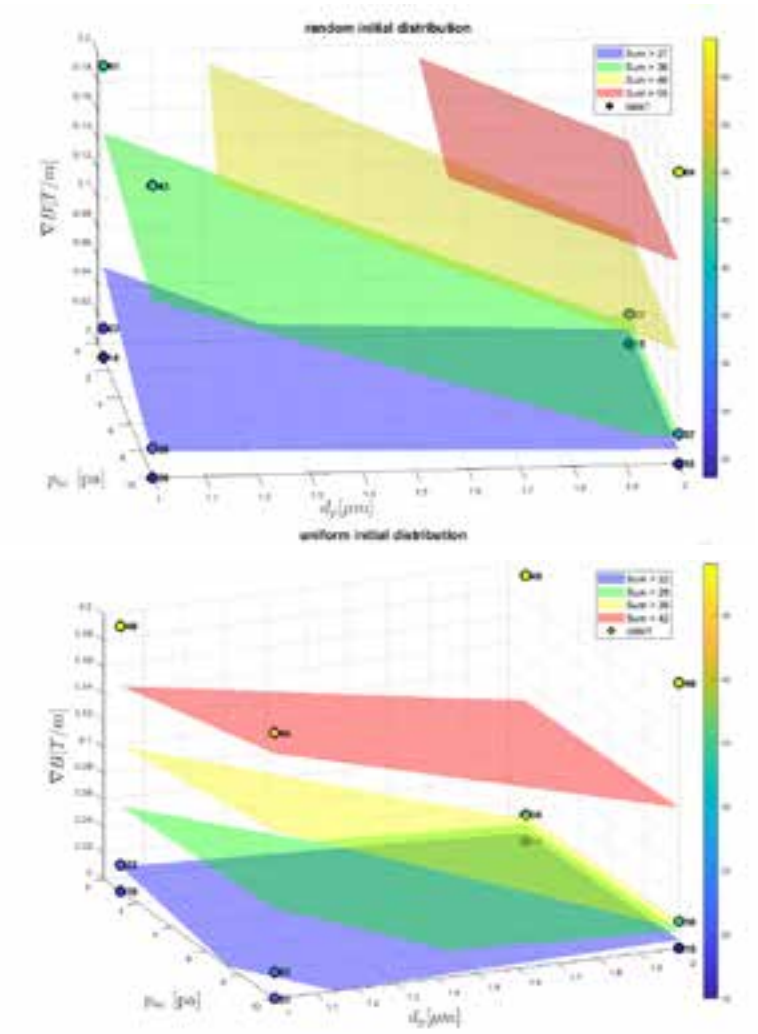

Figure 11: Parametric iso-surfaces: olfactory delivery efficiency versus particle size, acoustic pressure, and magnetic gradient

Particle size was found to be a critical factor in controlling the motion of nasally inhaled ferromagnetic drug particles. For the combined acoustic-magnetic approach, the optimal particle size was approximately 1-2 μm, which is larger than the optimal size for acoustic radiation alone (1-2 μm). This is because larger particles experience stronger magnetic forces due to their larger volume, while still being responsive to acoustic radiation forces.

The magnetic field strength, determined by the remanent magnetization of the permanent magnets, showed a strong positive correlation with olfactory delivery efficiency. Increasing the magnetic field strength from 0.04 T to 0.4 T resulted in an approximately linear increase in olfactory delivery efficiency from 50% to 65% for the combined approach.

The acoustic pressure amplitude also influenced the olfactory delivery efficiency, with higher amplitudes generally resulting in better performance. However, the effect plateaued above 2 Pa, suggesting that there is an optimal range of acoustic pressure for efficient olfactory delivery.

The release position of particles at the nostril inlet was found to be an important factor, with particles released closer to the superior portion of the nostril having a higher probability of reaching the olfactory region. This effect was more pronounced for the magnetic-only approach than for the combined approach, indicating that the combined approach is more robust to variations in release position.

The correlation between olfactory delivery efficiency and various parameters was analyzed using the Pearson correlation coefficient. The results showed that the product of the magnetic field gradient and the acoustic pressure gradient had the strongest correlation with olfactory delivery efficiency ($r = 0.87$), followed by the magnetic field gradient alone ($r = 0.76$) and the acoustic pressure gradient alone ($r = 0.68$). This suggests that the combined effect of both forces is indeed synergistic rather than merely additive.

Figure 11 presents parameter study iso surfaces which investigating olfactory particle entry from 10,000 initial particles reveals significant dependencies on particle size (d_p), inlet acoustic pressure (pin), and magnetic field gradient (∇B), with notable differences between uniform and random initial distributions. For uniform distribution, maximum particle counts ranged from 15 to 49, with optimal performance achieved at smaller particle sizes (d_p= 1 μm) combined with higher magnetic field gradient, yielding 49 particles. In contrast, random initial distribution demonstrated superior overall performance, with particle counts ranging from 18 to 64 and revealing a distinct optimal regime at larger particle sizes (d_p= 2 μm) with high magnetic field gradient, achieving the maximum of 64 particles—a 31% improvement over the uniform distribution optimum. The random distribution consistently outperformed uniform initialization across most parameter combinations, particularly for larger particles and higher magnetic field gradient, suggesting that stochastic initial conditions enhance particle transport efficiency to the olfactory region. Both distributions showed that magnetic field gradient exerted the strongest influence on particle delivery, followed by particle size, while inlet acoustic pressure (pin) exhibited more modest effects. These findings highlight the critical importance of initial particle distribution patterns in olfactory drug delivery systems and indicate that optimal parameter selection is distribution-dependent, with random initialization enabling more efficient particle transport, especially for larger particles at higher magnetic field gradient (∇B).

In summary, this complex figure visualizes the results of a multi-parameter sensitivity analysis. It uses iso-surfaces in a 3D parameter space, where the axes are key variables: particle size, inlet acoustic pressure, and magnetic field gradient. The surfaces represent contours of constant olfactory delivery efficiency. It visually reveals which parameter combinations yield the highest deposition (e.g., the “hilltop” in the plot). The discussion notes it shows the superior performance of random initial particle distribution and pinpoints the optimal regime: larger particles (~2 μm) under a high magnetic field gradient, achieving the maximum 64% efficiency.

The results of this study demonstrate that a combined approach using both acoustic radiation and magnetic forces can significantly enhance drug delivery to the olfactory region compared to either approach alone. This section discusses the key findings, their implications, and the limitations of the current study.

Interpretation of Acoustic Radiation Results

The results of this study suggested that the optimal frequency of sound waves emitted at the nostril for olfactory drug delivery was in the range 9-19 kHz. This result was

compiled from more than 8000 numerical deposition test cases of 8 terabytes in commercial software [72]. Four nasal geometries were evaluated in a wide frequency spectrum of 9000-19000 Hz. The reasons for the optimal frequency being 9-19 kHz in olfactory targeting may be explained as follows. As illustrated in Figure 3, valleys and peaks of the acoustic pressure exist inside the nasal cavity, which can act as a stabilizing or destabilizing force to collect or repel particles. In other words, the interactions between the nasal airway and input sound waves lead to either "friendly" zones, where the acoustic pressure gradients point to the olfactory region and help drive particles toward it, or "unfriendly" zones where the acoustic pressure gradients push particles away from the olfactory region. In Figure 4, a pressure valley (i.e., friendly zone) was observed that covered the upper-front nose and part of the olfactory region, with particles in the covered regions being more likely to deposit in the olfactory region. At higher frequencies (Figure 4), the acoustic pressure valleys/peaks are smaller and distributed in an alternating manner. An "unfriendly" zone in the proximity of the olfactory region can effectively block particles from reaching it. As a result, the total area of the "friendly" zones to the olfactory region did not constantly increase with the frequency but rather reached a peak around 11–15 kHz and decreased slightly at higher frequencies.

The predicted olfactory deposition fractions in this study (i.e., 0.6%) were lower than those in many previous studies. For instance, Schroeter et al. [57] measured the nasal deposition of 10.3 μm particles and reported a maximum olfactory deposition fraction of 5%. However, it is noted that olfactory dosing depends on the defined region that was designated as "olfactory region". In Schroeter et al. [57], the olfactory region included both the superior turbinate and the olfactory region. More importantly, local particle deposition in the nasal cavity is highly sensitive to the location of the nose due to its convoluted structure. Only a small fraction of drug particles can escape the filtration by the nasal valve and reach the turbinate; among them, even a much smaller fraction can change direction from the axial direction to move upward and reach the increasingly narrowed olfactory region. Xi et al. [58] compared the olfactory delivery efficiencies based on different definitions of the olfactory region and noted that the difference could be as large as one order of magnitude. As a result, a comparison of the olfactory deposition fractions among different studies should include how the targeted olfactory region was defined. Furthermore, the low olfactory deposition rates predicted in this study highlight the challenges of N2B drug delivery and call for more studies to investigate new delivery strategies to dispense drugs to this region.

Interpretation of Magnetic Force Results

The addition of magnetic forces to guide ferromagnetic particles to the olfactory region demonstrated significant improvements in delivery efficiency. The magnetic field gradient created by the permanent magnets provided directional control over particle trajectories, helping to overcome the challenges posed by the complex nasal geometry.

The single-magnet configuration, with a magnet positioned above the olfactory region, created a strong vertical magnetic field gradient that attracted particles upward toward the olfactory region. However, this configuration was limited by the rapid decay of magnetic field strength with distance, making it less effective for particles traveling in the lower portions of the nasal cavity. Additionally, particles in the anterior nasal region were still subject to inertial impaction and gravitational settling, resulting in significant deposition before reaching the olfactory region.

The dual-magnet configuration addressed these limitations by adding a second magnet at the front of the nasal cavity. This front magnet helped to guide particles past the nasal valve region, reducing deposition in the anterior nose. The particles were then attracted to the olfactory region by the top magnet. This configuration demonstrated improved performance compared to the single-magnet approach, with olfactory delivery efficiencies of 45-50% compared to 35-40% for the single-magnet configuration.

The effectiveness of magnetic guidance was found to be highly dependent on particle size and magnetic properties. Larger particles (1-2 μm) experienced stronger magnetic forces due to their larger volume, making them more responsive to magnetic guidance. However, very large particles (>1 μm) were more susceptible to inertial impaction and gravitational settling, reducing their ability to reach the olfactory region. The optimal particle size for magnetic guidance alone was found to be approximately 1-2 μm, which is larger than the optimal size for acoustic radiation alone (1-2 μm).

The magnetic susceptibility of the particles also played a crucial role in determining the effectiveness of magnetic guidance. Particles with higher magnetic susceptibility experienced stronger magnetic forces, resulting in better guidance to the olfactory region. However, highly magnetic particles tended to form aggregates due to magnetic dipole-dipole interactions, which could affect their aerodynamic behavior and deposition patterns. This effect was not explicitly modeled in the current study but should be considered in future investigations.

Synergistic Effects of Combined Acoustic-Magnetic Approach

The most significant finding of this study is the synergistic effect observed when combining acoustic radiation and magnetic forces. The combined approach achieved olfactory delivery efficiencies of 60-65%, which is substantially higher than either approach alone (45% for acoustic radiation, 50% for magnetic guidance).

This synergistic effect can be attributed to the complementary nature of the two forces. Acoustic radiation forces help to suspend particles in the airflow and prevent wall deposition, particularly in the anterior nasal region where inertial impaction is a dominant deposition mechanism. Magnetic forces, on the other hand, provide directional guidance toward the olfactory region, helping particles navigate the complex nasal geometry.

The optimal frequency range for the combined approach was found to be the same as for acoustic radiation alone (9–19 kHz), suggesting that the acoustic component of the combined approach functions similarly to the acoustic-only approach. However, the optimal particle size for the combined approach (1-2 μm) was larger than for acoustic radiation alone (1-2 μm), reflecting the stronger influence of magnetic forces on larger particles.

The correlation analysis revealed that the product of the magnetic field gradient and the acoustic pressure gradient had the strongest correlation with olfactory delivery efficiency ($r = 0.87$), further supporting the synergistic nature of the combined approach. This suggests that the two forces work together in a multiplicative rather than additive manner, potentially due to their orthogonal directions of action in many regions of the nasal cavity.

The iso-surfaces in Figure 11 are effectively "performance landscapes" in a 3D parameter space. Their shape reveals the *competing and cooperative physical forces* that govern particle transport, and explains the observed optimal regime for random vs. uniform initial distributions.

Axis Variables: Decoding the Forces

- Particle Size (dp): This is a master variable scaling multiple forces.

– Mass & Inertia: Scales with (dp3). Larger particles are harder to accelerate by flow or forces, and have greater momentum, making them more susceptible to inertial impaction on airway bends (a negative effect).

– Acoustic Radiation Force: For a given field, larger particles experience a stronger acoustic push/pull into pressure nodes/antinodes.

– Magnetic Force: Larger particles have a greater magnetic volume, making them far more responsive to magnetic guidance.

– Drag Force: Scales with (dp) as Stokes drag. Larger particles experience relatively less drag per unit of driving force compared to their inertia and magnetic/acoustic forces.

- Inlet Acoustic Pressure: Governs the intensity of the acoustic field. Higher (pin) increases the acoustic radiation force, creating stronger pressure gradients to structure the flow and suspend particles, countering gravitational settling and wall adhesion.
- Magnetic Field Gradient: Governs the strength and localization of the magnetic steering. Higher Magnetic Field Gradient creates a steeper "magnetic potential hill," producing a stronger, more directed pulling force toward the olfactory target.

Interpreting the Iso-Surface Topography

The study found a distinct optimal peak for random initial distribution at larger particles (~2 μm) and high (∇B), achieving 64% efficiency—a 31% improvement over the uniform distribution optimum.

- For very small particles (e.g., < 1 μm), the dominant force is drag from the background airflow. Their inertia is negligible, and while acoustic forces still act, magnetic force becomes vanishingly weak. They are essentially tracers of the bulk flow, which, due to nasal geometry,

has very low streamline penetration into the olfactory slit (~1%). The magnetic field cannot adequately steer them from the main flow path.

- The olfactory region is a small, recessed target. To pull a particle from the high-velocity central airstream into this low-flow zone requires a strong, localized force. A high (∇B) provides the necessary "magnetic tug" to overcome the particle's momentum and drag, inducing a cross-stream migration. The iso-surfaces likely show that efficiency increases steeply with (∇B), confirming its role as the primary directional control parameter.
- The Acoustic Pressure effect is "more modest." This is physically sound. The acoustic field's primary role is not direct steering to the olfactory region, but flow conditioning and particle suspension. It agitates the flow, disrupts laminar boundary layers, and uses radiation forces to keep particles aloft and migrating, preventing premature deposition in the anterior nose (nasal valve, turbinates). This creates a "mobilized cloud" of particles that is then more susceptible to magnetic capture. Beyond a sufficient (p_{in}) to achieve this mobilization, further increases yield diminishing returns—hence the plateau effect.

The shape of the performance landscape justifies the synergy:

1. **Acoustics creates opportunity:** It reduces losses in the front nose by suspending particles and mitigating inertial impaction.
2. **Magnetics seizes the opportunity:** It provides the targeted, directional force to capture the mobilized particles and divert them into the olfactory slit.
3. **Particle Size tunes the coupling:** At ~2 μm, particles are large enough for magnetic force to be dominant over drag for steering, yet not so large that inertia causes them to crash into walls before being steered.

Random Distribution Outperforms Uniform is a critical finding. A uniform release at the nostril assumes perfect, idealized device performance. A random release simulates a more realistic, stochastic spray from a nebulizer.

- Physical Justification: The nasal valve is the narrowest point and a major deposition site. A uniform front of particles will experience a high rate of collective impaction. A random, dispersed release means particles enter at different points in time and space. This desynchronizes their arrival at the nasal valve, reducing the "clogging" effect and allowing the magnetic field to act on particles sequentially. Some particles randomly released in favorable positions (e.g., closer to the superior meatus) have a much higher probability of being captured. The random distribution effectively samples a wider range of initial trajectories, and the magnetic "filter" then selects and guides the favorably positioned ones, leading to higher overall efficiency in a complex, chaotic transport process.

In conclusion, back to the Figure 11 is not just a result plot; it is a physical map of the force balance governing targeted nasal delivery. It proves that the combined system is not additive, but synergistic and condition-dependent, with magnetic guidance as the directional driver, acoustic mobilization as the enabler, particle size as the coupling factor, and initial distribution realism as a critical determinant of real-world efficacy.

Limitations and Future Directions

There are several assumptions that may limit the applicability of the results of this study. First, the inhalation flow was not considered, and the results of this study can only represent the scenarios of breath-holding or very slow breathing conditions. Second, only four nasal geometries were considered, which cannot represent the intra-subject or inter-subject variability. Moreover, three nasal geometries were generated by modifying a patient-specific nose model. More patient-specific models are needed to verify the generality of the results in this study. Third, fluid-structure interactions, as well as the nasal wall compliance, were neglected. Moreover, there were no benchmark experiments yet to validate the olfactory deposition under radiation forces. Future *in vitro* studies using 3D printed nasal casts can provide valuable data to improve the accuracy of the numerical model developed in this study. After saying this, the predominant physics (i.e., acoustic-particle-wall interactions) were considered here in anatomically accurate nasal geometries under acoustic radiation forces of a wide spectrum (f = 9000-19000 Hz). In doing so, the results of this study can be used as guidelines for future acoustic-aided intranasal olfactory drug delivery.

The addition of magnetic forces introduces additional complexities and limitations. The magnetic field strength decreases rapidly with distance from the magnet, limiting

the effective range of magnetic guidance. This could be particularly challenging for clinical applications where the magnets must be placed outside the body. Future studies could explore the use of stronger magnets, optimized magnet configurations, or even electromagnets with dynamic control to overcome these limitations. The current study also did not consider the potential biological effects of magnetic fields on nasal tissues or drug formulations. While the magnetic field strengths used in this study are generally considered safe for short-term exposure, long-term effects and potential interactions with specific drug formulations should be investigated before clinical application.

Another limitation is the assumption of spherical, monodisperse particles with uniform magnetic properties. In reality, drug particles may have irregular shapes, size distributions, and varying magnetic content, which could affect their aerodynamic and magnetic behavior. Future studies should incorporate more realistic particle models to better predict the performance of the combined approach in clinical settings. Despite these limitations, the results of this study provide valuable insights into the potential of a combined acoustic-magnetic approach for enhancing olfactory drug delivery. The significant improvement in delivery efficiency compared to conventional methods suggests that this approach could be a promising strategy for N2B drug delivery, potentially enabling more effective treatment of neurological disorders.

The most important limitation of this study is the absence of experimental validation. While the flow and acoustic submodels were individually validated against published data, the combined acoustic-magnetic deposition efficiency has not been measured in a physical nasal cast or animal model. Future work using 3D-printed nasal replicas with embedded acoustic transducers and external permanent magnets is strongly recommended as a direct next step before any clinical translation.

Clinical Translation, Safety, and Biocompatibility

The promising computational results of the combined acoustic-magnetic approach raise important considerations for clinical implementation, particularly regarding device integration, acoustic exposure safety, and biocompatibility of the magnetic particles. The dual-magnet configuration (anterior and superior placement) and the acoustic transducer (operating at 9–19 kHz) can be integrated into a handheld inhaler form factor without fundamental technical barriers. Existing commercial intranasal delivery devices, such as the Optinose pressurized olfactory delivery (POD) device, already demonstrate that directed aerosol administration to the upper nasal cavity is clinically achievable [34]. The POD device uses a bidirectional mechanism with a mouthpiece and a sealing nosepiece to exploit natural respiratory reflexes. Extending this concept, a next-generation device could incorporate: (i) a small piezoelectric acoustic emitter (e.g., a disc-type transducer with dimensions <20 mm diameter) mounted in the nosepiece or in the flow channel, driven by a compact power source (e.g., a rechargeable lithium-ion battery); and (ii) two small neodymium permanent magnets (grade N52, ~1 cm^3 each) placed externally on the device housing – one anteriorly near the nostril and one superiorly above the olfactory region. The magnets would not require active cooling or electrical connections, simplifying sterility and reuse considerations. The acoustic driver adds negligible weight (<10 g) and can be triggered only during the inhalation phase via a pressure sensor. Thus, the combined device would remain comparable in size and ergonomics to existing electronic inhalers (e.g., smart nebulizers). Future engineering work would need to optimize transducer positioning to avoid acoustic energy attenuation by the magnet housing, and to ensure that the magnetic field gradient at the olfactory region (0.04–0.2 T/m) is not compromised by the acoustic components. Nevertheless, the component technologies are mature, and the integration appears technically feasible for a clinical prototype.

The acoustic pressure amplitude applied at the nostril inlet in this study was 1 Pa, which corresponds to a sound pressure level (SPL) of approximately 94 dB re 20 µPa. This level is below the World Health Organization (WHO) occupational noise exposure limit of 85 dB A for an 8-hour work shift [WHO, 2018] and far below the 140 dB peak pressure threshold for immediate acoustic trauma. Critically, the exposure duration during a single intranasal drug delivery maneuver is very brief – approximately 2 seconds of steady inhalation at 15 L/min. Even for a therapeutic regimen of four actuations per day (morning and evening, two puffs each), the total daily acoustic exposure time would be ~8 seconds, which is negligible compared to established hazard thresholds. However, two specific safety aspects require attention:

1. **Auditory perception and annoyance:** The frequency range of 9–19 kHz lies partially within the human audible spectrum (upper limit ~20 kHz in young healthy adults). Frequencies above ~15 kHz may be inaudible to many adults due to presbycusis, but lower frequencies (9–12 kHz) are clearly audible and could cause patient discomfort or startle. Therefore, clinical devices should incorporate temporal gating – limiting acoustic emission to the precise inhalation window (2 s) and ramping the amplitude to avoid abrupt onset. Additionally, patients and healthcare providers should be informed of the audible nature of the device; a simple instruction to swallow or perform a Valsalva maneuver during emission may reduce annoyance.
2. **Hearing protection assessment:** Although the exposure is short, patients with pre-existing hearing loss, tinnitus, or hyperacusis may be more sensitive. For routine clinical use, no specialized hearing protection (e.g., earplugs) is likely necessary given the low SPL and short duration. However, for pediatric populations or repeated daily use over many years, a conservative risk assessment would be prudent. This could include measuring the actual SPL at the tympanic membrane (which is attenuated by the nasal–pharyngeal–eustachian tube pathway) and confirming that the effective cochlear exposure is well below safe limits. If concerns remain, a passive muff or earplug could be offered to sensitive individuals without affecting drug delivery. Alternatively, shifting the operating frequency above 15 kHz (still within the 9–19 kHz range studied) would render it inaudible to most adults while retaining comparable acoustic radiation forces, as shown in the frequency analysis (Section 3.1). In summary, the acoustic parameters used in this simulation are safe for brief, controlled inhalation maneuvers, but device design should include user notification, amplitude ramping, and optionally frequency tuning to minimize annoyance.

The proposed approach relies on ferromagnetic particles with diameters of 1–2 μm and magnetic susceptibility typical of iron oxide (magnetite, Fe_3O_4). Several lines of evidence support the biocompatibility of such particles at the doses relevant to olfactory delivery:

- **FDA-approved formulations:** Ferumoxytol (Feraheme®) is an intravenous iron oxide nanoparticle formulation approved by the U.S. Food and Drug Administration for the treatment of iron deficiency anemia in patients with chronic kidney disease. Although ferumoxytol particles are smaller (17–31 nm) than the 1–2 μm particles simulated here, its safety profile (infusion reactions, hypotension, and rare anaphylaxis) is well characterized, and no significant long-term organ toxicity has been observed at therapeutic iron doses. Larger microparticles (1–10 μm) composed of magnetite have been evaluated in preclinical models for magnetic drug targeting and shown to be well tolerated when deposited in the respiratory tract, provided they are biodegradable and cleared by alveolar macrophages [38].
- **Safety literature:** Häfeli and Pauer [38] systematically reviewed the *in vitro* and *in vivo* toxicity of magnetic microspheres, concluding that properly coated iron oxide particles (e.g., with starch, albumin, or polyethylene glycol) exhibit low cytotoxicity and are cleared from the body via the reticuloendothelial system. Pankhurst et al. [39] provided a comprehensive overview of biomedical applications of magnetic nanoparticles, emphasizing that iron oxides are generally biocompatible and that the main risks (oxidative stress, inflammatory response) are dose-dependent. For intranasal delivery to the olfactory region, the predicted deposited dose is on the order of micrograms to low milligrams per administration (based on the 60–65% delivery efficiency from 10,000 particles of 1 μm diameter). This is orders of magnitude lower than the intravenous doses of ferumoxytol (up to 510 mg iron per dose) and well within the safety margins established in animal studies.
- **Mucociliary clearance and metabolism:** Particles deposited in the olfactory region may be transported either directly into the brain parenchyma via the olfactory nerve pathway or cleared by the mucociliary apparatus toward the nasopharynx and subsequently swallowed. Iron oxide particles in the 1–2 μm range are known to be phagocytosed by macrophages and gradually degraded into ferritin or hemosiderin, entering the body's normal iron. No specific toxicity has been attributed to intranasal iron oxide deposition at these low doses. Nevertheless, a dedicated toxicokinetic study using a relevant animal model (e.g., rat or rabbit) would be necessary before first-in-human trials.

Particle aggregation: One acknowledged challenge is the tendency of ferromagnetic particles to form aggregates due to magnetic dipole–dipole interactions, especially at higher magnetic field gradients. This effect was not explicitly modeled in the present study but could alter the effective aerodynamic diameter and reduce delivery efficiency. Aggregation may also increase the risk of embolic phenomena if particles were to enter the bloodstream via the nasal mucosa. However, the olfactory epithelium is not highly vascularized, and particles entering the brain parenchyma would be isolated from the systemic circulation. For future investigations, we recommend (i) using particles with a non-magnetic coating (e.g., silica or polymer) to reduce aggregation while preserving magnetic responsiveness, and (ii) performing *in vitro* aggregation studies under simulated flow and field conditions to guide the selection of optimal particle formulations. Surface functionalization with polyethylene glycol (PEG) or dextran has been shown to minimize aggregation and improve colloidal stability [39].

In conclusion, the combined acoustic-magnetic approach is clinically feasible with existing component technologies, acoustically safe for brief inhalation maneuvers (with minor user-interface considerations), and compatible with well-studied iron oxide particles that have regulatory precedent. The next translational steps should include benchtop prototyping of the integrated device, *in vitro* deposition testing in a 3D-printed nasal cast, and acute safety studies in a large animal model.

CONCLUSIONS

A commercial software-based computational model for acoustic-aided and magnetically-guided olfactory drug delivery was developed in four nasal geometries. A systematic parametric study of the acoustophoretic and magnetophoretic guidance to the olfactory region was performed for frequencies of 9000-19000 Hz at a resolution of 50 Hz and various magnetic field configurations. Findings were extracted from multi-terabyte computational results that could be used as guidelines for future acoustic-magnetic-aided intranasal olfactory drug delivery. These simulation-based findings offer preliminary quantitative guidelines with major findings are:

(1) Frequency analyses of the nasal cavity revealed that certain eigenfrequencies were particularly associated with the olfactory region and had the potential to deliver more drugs to the olfactory region.

(2) At high frequencies, the acoustic pressure peaks/valleys were smaller in size and distributed in an alternating manner.

(3) Turbinate shrinking/swelling did not have a significant impact on the magnitude of the olfactory delivery efficiency but would alter the frequency for optimal olfactory delivery.

(4) The olfactory deposition was maximal at 11–15 kHz and decreased at higher frequencies. The olfactory deposition was almost constant for higher frequencies.

(5) Magnetic forces provided directional control over particle trajectories, with the dual-magnet configuration shows computational promise for enhancing N2B drug delivery outperforming the single-magnet approach.

(6) The combined acoustic-magnetic approach demonstrated synergistic effects, achieving olfactory delivery efficiencies of 60-65%, substantially higher than either approach alone (45% for acoustic radiation, 50% for magnetic guidance).

(7) A higher cross-correlation between the product of pressure and pressure gradient and the olfactory deposition delivery efficiency was found than other acoustic parameters. The nearest peaks belong to the y component of local acceleration, and the minimum unnormalized distance based on dynamic time warping algorithm belongs to the total acoustic pressure field.

(8) Frequency analysis near the olfactory region showed a negative correlation between acoustic pressure and turbinate cross-section.

(9) The optimal particle size for the combined approach (1-2 μm) was larger than for acoustic radiation alone (1-2 μm), reflecting the stronger influence of magnetic forces on larger particles.

(10) The product of the magnetic field gradient and the acoustic pressure gradient had the strongest correlation with olfactory delivery efficiency ($r = 0.87$), supporting the synergistic nature of the combined approach.

This study demonstrates that a combined acoustic-magnetic approach offers a promising strategy for enhancing N2B drug delivery, potentially enabling more effective treatment of neurological disorders. Future work should focus on experimental validation, optimization of magnetic field configurations, and investigation of the biological effects of the combined approach. The combined acoustic-magnetic approach achieves up to 65% olfactory delivery efficiency, representing a ~30–44% relative improvement over either force alone, with optimal performance at 11–15 kHz, 1–2 μm particles, and a dual-magnet configuration. Below in table 4 the most important conclusions of the paper, extracted and summarized.

Table 4: Study summarization and implication

Field	Key Finding	Quantitative Result	Implication
Optimal frequency range	Acoustic delivery to olfactory region is maximized at specific eigenfrequencies.	9–19 kHz (peak at 11–15 kHz)	Higher frequencies produce smaller alternating pressure peaks/valleys that can block particle transport.
Acoustic-only delivery	Maximum olfactory deposition using acoustic radiation alone.	~45%	Baseline for comparison; limited by anterior nasal deposition.
Magnetic-only (single magnet)	Vertical field gradient above olfactory region attracts particles upward.	35–40%	Limited by rapid field decay and anterior deposition.
Magnetic-only (dual magnet)	Front magnet guides particles past nasal valve; top magnet directs to olfactory region.	45–50%	Improved over single magnet by reducing anterior loss.
Combined acoustic-magnetic	Synergistic effect: acoustic suspension + magnetic steering.	60–65%	Substantially higher than either method alone (45% and 50%).
Optimal particle size	Balance between magnetic responsiveness and inertial impaction.	1–2 μm	Larger than optimal for acoustics alone (1–2 μm); magnetic force scales with volume.
Magnetic field gradient effect	Strong positive correlation with delivery efficiency.	0.04–0.4 T/m → 50% → 65%	Near-linear increase; product with acoustic gradient yields strongest correlation (r = 0.87).
Acoustic pressure amplitude	Higher amplitude improves efficiency, but with diminishing returns.	Plateau above 2 Pa	Modest effect compared to magnetic gradient.
Release position / distribution	Random initial distribution outperforms uniform distribution.	31% relative improvement (64 vs. 49 particles per 10,000)	Stochastic release samples favorable trajectories; magnetic filter selects optimally positioned particles.
Influence of turbinate size	Shrinking/swelling alters optimal frequency but not maximum efficiency magnitude.	Frequency shift, efficiency ~constant	Anatomical variation requires frequency tuning, but peak performance remains achievable.
Correlation analysis	Combined parameter ($\nabla B \times \nabla p$) has highest correlation with olfactory deposition.	r = 0.87	Supports synergistic (multiplicative) rather than additive interaction.
Impact of nasal geometry	Four different MRI-based geometries showed consistent trends but different eigenfrequencies.	Real eigenfrequencies: 182–360 Hz; imaginary: 582–618 Hz	Anatomical variability must be considered in device design.

ACKNOWLEDGEMENTS

Funding

This research received no external funding.

Data Availability Statement

The data presented in this study are available on request from the corresponding author.

Conflicts of Interest

The authors declare no conflict of interest.

Ethical Statement for MRI Data Usage

The nasal cavity geometries used in this study were reconstructed from magnetic resonance imaging (MRI) scans of four healthy adult volunteers (two males and two females, aged 34–50 years). All participants provided written informed consent prior to imaging. The study protocol, including data acquisition and anonymization procedures, was approved by the Institutional Review Board (IRB). All methods were performed in accordance with the relevant guidelines and regulations of the Declaration of Helsinki. MRI data were anonymized and de-identified prior to reconstruction, ensuring that no personally identifiable information was retained or used in the computational models. No additional patient data or clinical interventions were involved.

RESEARCH METHODOLOGY

1. Gooch CL, Pracht E, Borenstein AR. (2017). The burden of neurological disease in the United States: A summary report and call to action. Annals of Neurology. 81(4):479-484.
2. GBD 2016 Parkinson's Disease Collaborators. (2018). Global, regional, and national burden of Parkinson's disease, 1990–2016: A systematic analysis for the Global Burden of Disease Study 2016. The Lancet. Neurology. 17:939-953.
3. Polanczyk GV, Willcutt EG, Salum GA, Kieling C, Rohde LA. (2014). ADHD prevalence estimates across three decades: An updated systematic review and meta-regression analysis. International Journal of Epidemiology. 43:434-442.
4. Baxter AJ, Brugha TS, Erskine HE, Scheurer RW, Vos T, Scott JG. (2015). The epidemiology and global burden of autism spectrum disorders. Psychological Medicine. 45(3):601-613.
5. Maenner MJ, Warren Z, Williams AR, Amoakohene E, Bakian AV, Bilder DA, et al. (2016). Prevalence and characteristics of autism spectrum disorder among children aged 8 years—Autism and developmental disabilities monitoring network, 11 sites, United States, 2012. MMWR. Surveillance Summaries. 65:1–23.
6. GBD 2016 Neurology Collaborators. (2019). Global, regional, and national burden of neurological disorders, 1990–2016: A systematic analysis for the Global Burden of Disease Study 2016. The Lancet. Neurology. 18(5):459-480.
7. Pardridge WM. (2005). The blood-brain barrier: Bottleneck in brain drug development. NeuroRx. 2(1):3-14.
8. Hanson LR, Frey WH 2nd. (2008). Intranasal delivery bypasses the blood-brain barrier to target therapeutic agents to the central nervous system and treat neurodegenerative disease. BMC Neuroscience. Suppl 3(Suppl 3):S5.
9. Lochhead JJ, Thorne RG. (2012). Intranasal delivery of biologics to the central nervous system. Advanced Drug Delivery Reviews. 64:614-628.
10. Dhuria SV, Hanson LR, Frey WH 2nd. (2010). Intranasal delivery to the central nervous system: Mechanisms and experimental considerations. Journal of Pharmaceutical Sciences. 99(4):1654-1673.
11. Craft S, Baker LD, Montine TJ, Minoshima S, Watson GS, Claxton A, et al. (2012). Intranasal insulin therapy for Alzheimer disease and amnestic mild cognitive impairment: A pilot clinical trial. Archives of Neurology. 69(1):29-38.
12. Francis GJ, Martinez JA, Liu WQ, Xu K, Ayer A, Fine J, et al. (2008). Intranasal insulin prevents cognitive decline, cerebral atrophy and white matter changes in murine type I diabetic encephalopathy. Brain. 131(Pt 12):3311-3334.
13. Fine JM, Forsberg AC, Stroebel BM, Faltesek KA, Verden DR, Hamel KA, et al. (2012). Intranasal deferoxamine affects memory loss, oxidation, and the insulin pathway in the streptozotocin rat model of Alzheimer's disease.

Journal of the Neurological Sciences. 321:100–111.

14. Chen XQ, Fawcett JR, Rahman YE, Ala TA, Frey II WH. (1998). Delivery of nerve growth factor to the brain via the olfactory pathway. Journal of Alzheimer's disease. 1:35-44.

15. Frey WH, Liu J, Chen X, Thorne RG, Fawcett JR, Ala TA, Rahman YE. (1997). Delivery of 125I-NGF to the brain via the olfactory route. Drug Delivery. 4(2):87-92.

16. Mistry A, Stolnik S, Illum L. (2009). Nanoparticles for direct nose-to-brain delivery of drugs. International Journal of Pharmaceutics. 379:146-157.

17. Illum L. (2003). Nasal drug delivery—Possibilities, problems and solutions. Journal of Controlled Release. 87(1-3):187–198.

18. Kooiman K, Vos HJ, Versluis M, de Jong N. (2014). Acoustic behavior of microbubbles and implications for drug delivery. Advanced Drug Delivery Reviews. 72:28-48.

19. Ye D, Sultan D, Zhang X, Yue Y, Heo GS, Kothapalli SVVN, et al. (2020). Focused ultrasound-enabled delivery of radiolabeled nanoclusters to the pons. Journal of Controlled Release. 328:127–135.

20. Schroeter JD, Kimbell JS, Asgharian B. (2006). Analysis of particle deposition in the turbinate and olfactory regions using a human nasal computational fluid dynamics model. Journal of Aerosol Medicine. 19:301–313.

21. Xi J, Berlinski A, Zhou Y, Greenberg B, Ou X. (2012). Breathing resistance and ultrafine particle deposition in nasal–laryngeal airways of a newborn, an infant, a child, and an adult. Annals of Biomedical Engineering. 40(12):2579–2595.

22. Cheng YS, Holmes TD, Gao J, Guilmette RA, Li S, Surakitbanharn Y, et al. (2001). Characterization of nasal spray pumps and deposition pattern in a replica of the human nasal airway. Journal of Aerosol Medicine. 14(2):267–280.

23. Inthavong K, Tian ZF, Tu JY, Yang W, Xue C. (2008). Optimising nasal spray parameters for efficient drug delivery using computational fluid dynamics. Computers in Biology and Medicine. 38(6):713–726.

24. Xi J, Yuan JE, Zhang Y, Nevorski D, Wang Z, Zhou Y. (2016). Visualization and quantification of nasal and olfactory deposition in a sectional adult nasal airway cast. Pharmaceutical Research. 33(6):1527–1541.

25. Xi J, Zhang Z, Si XA. (2015). Improving intranasal delivery of neurological nanomedicine to the olfactory region using magnetophoretic guidance of microsphere carriers. International journal of Nanomedicine.10:1211–1222.

26. Xi J, Zhang Z, Si XA, Yang J, Deng W. (2016). Optimization of magnetophoretic-guided drug delivery to the olfactory region in a human nose model. Biomechanics and Modeling in Mechanobiology. 15(4):877–891.

27. Bernad SI, Bernad E. (2022). Magnetic Forces by Permanent Magnets to Manipulate Magnetoresponsive Particles in Drug-Targeting Applications. Micromachines.13(11):1818.

28. Zhang Z, Xi J, Si XA, Yang J. (2019). Computational investigation of microparticle transport and deposition in the nasal cavity under unsteady airflows. J. Aerosol Sci. 129:71–81.

29. Kimbell JS, Segal RA, Asgharian B, Wong BA, Schroeter JD, Southall JP, et al. (2007). Characterization of deposition from nasal spray devices using a computational fluid dynamics model of the human nasal passages. Journal of Aerosol Medicine. 20(1):59-74.

30. Inthavong K, Ge QJ, Se CMK, Yang W, Tu JY. (2011). Simulation of sprayed particle deposition in a human nasal cavity including a nasal spray device. Journal of Aerosol Medicine. 42:100-113.

31. Schroeter JD, Garcia GJM, Kimbell JS. (2011). Effects of surface smoothness on inertial particle deposition in human nasal models. Journal of Aerosol Medicine. 42:52-63.

32. Azarmi S, Roa WH, Löbenberg R. (2008). Targeted delivery of nanoparticles for the treatment of lung diseases. Advanced Drug Delivery Reviews. 60(8):863-875.

33. Salade L, Wauthoz N, Goole J, Amighi K. (2019). How to characterize a nasal product. The state of the art of in vitro and ex vivo specific methods. International Journal of Pharmaceutics. 561:47-65.

34. Djupesland PG. (2013). Nasal drug delivery devices: Characteristics and performance in a clinical perspective—A review. Drug Delivery and Translational Research. 3(1):42-62.

35. Kundoor V, Dalby RN. (2010). Assessment of nasal spray deposition pattern in a silicone human nose model using a color-based method. Pharmaceutical Research. 27(1):30-36.

36. Grief AD, Richardson G. (2005). Mathematical modelling of magnetically targeted drug delivery. Journal of Magnetism and Magnetic Materials. 293:455-463.

37. Dames P, Gleich B, Flemmer A, Hajek K, Seidl N, Wiekhorst F, et al. (2007). Targeted delivery of magnetic aerosol droplets to the lung. Nature Nanotechnology. 2(8):495-499.

38. Häfeli UO, Pauer GJ. (1999). In vitro and in vivo toxicity of magnetic microspheres. Journal of Magnetism and Magnetic Materials. 194:76–82.

39. Pankhurst QA, Connolly J, Jones SK, Dobson J. (2003). Applications of magnetic nanoparticles in biomedicine. Journal of Physics D: Applied Physics. 36:R167–R181.

40. Alexiou C, Arnold W, Klein RJ, Parak FG, Hulin P, Bergemann C, et al. (2000). Locoregional cancer treatment with magnetic drug targeting. Cancer Research. 60(23):6641-6648.

41. Alexiou C, Arnold W, Klein RJ, Parak FG, Hulin P, Bergemann C, et al. (1996). Clinical experiences with magnetic drug targeting: A phase I study with 4′-epidoxorubicin in 14 patients with advanced solid tumors. Cancer Res. 56:4686-4693.

42. Shapiro B, Kulkarni S, Nacev A, Muro S, Stepanov PY, Weinberg IN, et al. (2015). Open challenges in magnetic drug targeting. Wiley Interdisciplinary Reviews. Nanomedicine and Nanobiotechnology. 7(3):446-457.

43. Nacev A, Beni C, Bruno O, Shapiro B. (2011). The behaviors of ferromagnetic nano-particles in and around blood vessels under applied magnetic fields. Journal of Magnetism and Magnetic Materials. 323(6):651-668.

44. Sarwar A, Nemirovski A, Shapiro B. (2012). Optimal Halbach permanent magnet designs for maximally pulling and pushing nanoparticles. Journal of Magnetism and Magnetic Materials. 324(5):742-754.

45. Tehrani MD, Yoon JH, Kim MO, Yoon J. (2015). A novel scheme for nanoparticle steering in blood vessels using a functionalized magnetic field. IEEE transactions on Bio-Medical Engineering. 62(1):303–313.

46. Kenjereš, S.; Righolt, B.W. (2012). Simulations of magnetic capturing of drug carriers in the brain vascular system. International Journal of Heat and Fluid Flow. 35:68-75.

47. Haverkort JW, Kenjereš S, Kleijn CR. (2009). Computational simulations of magnetic particle capture in arterial flows. Annals of Biomedical Engineering. Eng. 37(12):2436-2448.

48. Cherry EM, Maxim PG, Eaton JK. (2010). Particle size, magnetic field, and blood velocity effects on particle retention in magnetic drug targeting. Medical Physics. 37(1):175-182.

49. Furlani EP, Furlani EJ. (2007). A model for predicting magnetic targeting of multifunctional particles in the microvasculature. Journal of Magnetism and Magnetic Materials. 312(1):187-193.

50. Furlani EP. (2010). Magnetic biotransport: Analysis and applications. Materials. 3(4):2412–2446.

51. Furlani EP, Ng KC. (2006). Analytical model of magnetic nanoparticle transport and capture in the microvasculature. Physical review. E, Statistical, nonlinear, and soft matter physics. 73(6 Pt 1):061919.

52. Furlani EP, Xue X. (2012). A model for predicting field-directed particle transport in the magnetofection process. Pharmaceutical Research. 29(5):1366-1379.

53. Furlani EP, Xue X. (2012). Field, force and transport analysis for magnetic particle-based gene delivery. Microfluid. Nanofluidics. 13:589-602.

54. Rotariu O, Strachan NJC. (2005). Modelling magnetic carrier particle targeting in the tumor microvasculature for cancer treatment. Journal of Magnetism and Magnetic Materials. 293:639–646.

55. Cao Q, Han X, Li L. (2014). Configurations and control of magnetic fields for manipulating magnetic particles in microfluidic applications: Magnet systems and manipulation mechanisms. Lab Chip. 14(15):2762-2777.

56. Cao Q, Han X, Li L. (2011). Enhancement of the efficiency of magnetic targeting for drug delivery: Development and evaluation of magnet system. Journal of Magnetism and Magnetic Materials. 323(15):1919-1924.

57. Schroeter JD, Kimbell JS, Asgharian B, Tewksbury EW, Singal M. (2012). Computational fluid dynamics simulations of submicrometer and micrometer particle deposition in the nasal passages of a Sprague–Dawley rat. Journal of Aerosol Science. 43:31-44.

58. Xi J, Si XA, Kim J, Zhang Y, Jacob RE, Kabilan S, et al. (2016). Anatomical details of the rabbit nasal passages and their implications in breathing, air conditioning, and olfaction. The Anatomical Record. 299(7):853–868.

59. Pourmehran O, Arjomandi M, Cazzolato B, Tian Z, Inthavong K. (2020). The impact of geometric features on the particle deposition in the nasal passage. Journal of Aerosol Science. 140:105478.

60. Inthavong K, Shang Y, Tu J. (2014). Surface mapping for visualization of wall stresses during inhalation in a human nasal cavity. Respiratory Physiology Neurobiology. 190:54-61.

61. He Y, Yang T, Chen J, Shi W, Shi J. (2025). Insights Into Retronasal Sensation of Sweeteners Within Aerosol Particles Via Scalp Electroencephalogram. Sensory Neuroscience. 1:e70010.

62. Wang B, Wang L, Yang Q, Zhang Y, Qinglai T, Yang X, et al. (2024). Pulmonary inhalation for disease treatment: Basic research and clinical translations. Materials Today Bio. 25:100966.

63. Chaudhary S, Rawat S, Mathur S, Perveen A, Hafeez A, Bilgrami AL, et al. (2025). Next-generation neurotherapeutics: nanotechnology, immunotherapy, and gene editing for neurodegenerative diseases. Neurodegenerative Disease Management. 15(6):341-359.

64. Jamalabadi MYA. (2020). Frequency analysis and control of sloshing coupled by elastic walls and foundation with smoothed particle hydrodynamics method. Journal of Sound and Vibration. 476:115310.

65. Jiang Y, Fay JM, Poon CD, Vinod N, Zhao Y, Bullock K, et al. (2017). Nanoformulation of Brain-Derived Neurotrophic Factor with Target Receptor-Triggered-Release in the Central Nervous System. Advanced Functional Materials. 28(6):1703982.

66. Kumar R, Aadil KR, Mondal K, Mishra YK, Oupicky D, Ramakrishna S, et al. (2021). Neurodegenerative disorders management: state-of-art and prospects of nano-biotechnology. Critical Reviews in Biotechnology. 42(8):1180–1212.

67. Abdollahzadeh Jamalabadi MY. (2015). Entropy generation in boundary layer flow of a micro polar fluid over a stretching sheet embedded in a highly absorbing medium. Front. Heat Mass Transf. 6:7.

68. Lin MT, Chan TY, Liao WH, Wu CH, Young TH, Chen WS, et al. (2025). Low-Intensity ultrasound facilitation of intranasal drug delivery to olfactory bulb and trigeminal nerves. Ultrasound Med. Biol. 51(5):788–796.

69. Guo G, Zhang L, Ren H, Ding Y, Zhang Y, Tong Z, et al. (2024). Nasal drug delivery to olfactory region based on high-flow auxiliary gas method: A numerical simulation study. Powder Technology. 452:120567.

70. Khan AR, Liu M, Khan MW, Zhai G. (2017). Progress in brain targeting drug delivery system by nasal route. Journal of controlled release. 268:364–389.

71. Melaaen M, Reimers M, Røtnes JM, Aurdal L, Djupesland PG, et al. (2005). Using Computational fluid dynamics (CFD) to improve the Bi-Directional Nasal Drug Delivery concept. Food and Bioproducts Processing. 83(2):107-117.

72. COMSOL AB. COMSOL Multiphysics Reference Manual, version 6.4, 2025.